June 2018

Simulation of Radiation Flux from Thermal Fluid in Origami Tubes

Robert R. Bebeau
University of South Florida, rbebeau@mail.usf.edu

Simulation of Radiation Flux from Thermal Fluid in Origami Tubes

by

Robert R. Bebeau

A thesis submitted in partial fulfillment
of the requirements for the degree of
Master of Science in Mechanical Engineering
Department of Mechanical Engineering
College of Engineering
University of South Florida

Major Professor: Rasim Guldiken, Ph.D.
Diego Andrade, Ph.D.
Andres Tejada-Martinez, Ph.D.

Date of Approval:
June 18, 2018

Keywords: Thermal Management, Cavity Effect,
Spacecraft, Computational Fluid Dynamics, Heat Transfer

DEDICATION

I would like to dedicate this work to my mother, Christy Bebeau.

ACKNOWLEDGMENTS

I would like to thank Dr. Diego Andrade for first introducing me to the challenge discussed in this thesis, as well as for his instruction as a professor. He always encouraged me to push boundaries and explore the limits of learning. The guidance of Dr. Rasim Guldiken was invaluable during my time at the University of South Florida. Not only did he guide me through the thesis process, but he was also an excellent professor and department advisor. I would also like to thank Dr. Andres Tejada-Martinez. His insights helped direct my work on this thesis. I would like to extend my thanks to Catherine Burton, who helped me through the formatting of this manuscript and navigating the university procedures. Finally, I would like to thank my family, who have supported me during my graduate degree.

TABLE OF CONTENTS

LIST OF TABLES

LIST OF FIGURES

v

ABSTRACT

Spacecraft in orbit experience temperature swings close to 240 K as the craft passes from the shadow of the Earth into direct sunlight. To regulate the craft's internal energy, large radiators eject unwanted energy into space using radiation transfer. The amount of radiation emitted is directly related to the topology of the radiator design. Deformable structures such as those made with origami tessellation patterns offer a mechanism to control the quantity of energy being emitted by varying the radiator shape. Three such patterns, the Waterbomb, Huffman Waterbomb, and Huffman Stars-Triangles, can be folded into tubes. Origami tubes offer greater control and simplicity of design than flat radiators. Using FLUENT, Origami Simulator, and Solidworks to first simulate and then analyze the flow of a thermal fluid through the patterns and the radiation emitted from the created bodies, it was determined that the Waterbomb pattern achieved a 17.6 percent difference in emitted radiation, over a 2 percent change in fold. The Huffman Waterbomb pattern displayed a 42.7 percent difference in emitted radiation over a 20 percent change of fold. The simulations demonstrated both the feasibility and benefits of the origami designed tubes.

CHAPTER 1: INTRODUCTION

1.1 Objective and Scope

Energy emitted via radiation is dependent fundamentally on the topology of the radiating surface, specifically the presence of surfaces that face each other at steep angles. This dependence is caused by the cavity effect [1]. My objective for this thesis was to simulate the radiation flux emitted from the walls of origami tubes with a thermal fluid passing within them. I analyzed three origami patterns that each exhibit large cavities when folded (the Waterbomb, Huffman Waterbomb, and Huffman Stars-Triangles). The tubes were simulated to be in a vacuum, so radiation was the only mechanism available for heat dissipation. The three patterns were simulated through a range of boundary temperatures likely to be encountered in use, as well as over a range of fold percentages. In this thesis, I describe and analyze the simulations, the aspects of fluid dynamics, and heat transfer of origami tubes as proof of concept for using them as radiators for spacecraft.

1.2 Motivation

Thermal management of spacecraft is the principle application for thermal fluid-filled origami tubes. As a spacecraft orbits the Earth, it moves in and out of Earth's shadow and experiences cycles of direct sunlight and darkness, corresponding to ambient temperatures ranging from 153 K to 394 K [2,3]. Currently, spacecraft disperse internally-generated energy using flat plates with thermal fluid running in tubes between the plates [4]. Replacing this design with origami tubes containing thermal fluid both adds a mechanism that controls emitted radiation and simplifies the design.

1

1.3 Overview

The outline of this thesis follows:

- Chapter 2 presents the background. This includes all the necessary theory, equations, and models.

- Chapter 3 discusses the selection of geometries and the process of creating the solid bodies.

- Chapter 4 covers how meshes were generated.

- Chapter 5 presents the use of FLUENT in solving the models presented in Chapter 2.

- Chapter 6 discusses the results of the simulations.

- Chapter 7 presents the conclusions and proposes future works.

- Chapter 8 summarizes the contributions made by this thesis.

2

CHAPTER 2: BACKGROUND

This chapter provides context for the problem discussed in this thesis: a radiator based on origami tubes, and the motivation behind the work. It also contains relevant information on spacecraft, space science, heat transfer, origami designs, and fluid mechanics.

2.1 Motivational Background

Spacecraft in orbit are subjected to a wide range of ambient temperatures as they orbit the Earth. In the shadow of the Earth, the temperature can be as low as 153 K, while in the direct sunlight, the outside temperature rises to 394 K [2,3]. The temperature that a spacecraft will reach depends on a number of factors, including its size, shape, mass, material, and optical properties [3]. Some spacecraft, such as the International Space Station (ISS), are insulated to prevent the spacecraft from either burning up in the sunlight or freezing in the shadow of the Earth. This insulation also traps energy inside the spacecraft, so thermal management systems must be used to expel internally generated energy (from onboard equipment or personal) into space. The only way to expel excess heat is to radiate it into space. Therefore, spacecraft, such as (ISS), use flat plates to radiate the energy [4]. The energy is delivered to these plates via pipes containing a thermal fluid, specifically, liquid ammonia [4].

Figure 2.1 is an image of the radiator from the Early External Active Thermal Control System (EEATCS) that was used on the ISS [4]. The EEATCS radiator consists of an array of six

3

sets of radiator plates connected by hinges. Thermal fluid is run between each set of plates. The entire array is 13.6 m x 3.12 m. The radiator and accompanying system can eject 35 kW [4].
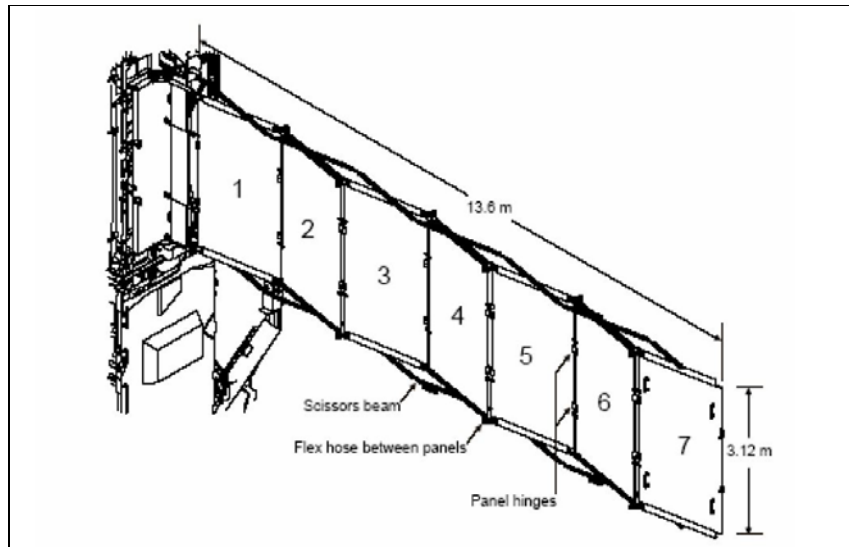
Figure 2.1 Diagram of the EEATCS radiator. Diagram adapted from [3].

Not all spacecraft are thermally insulated. Some rely solely on radiators to disperse both incident heat as well as internally generated energy while in the sunlight. In the shadow of the Earth, onboard heaters must be used to keep the spacecraft at operational temperatures [3]. In this case, external radiators are a hindrance as they will continue to radiate energy delivered by conduction.

In addition to changing external temperatures, most spacecraft have a range of operating conditions, generating differing amounts of internal energy, but most radiator designs are static. In other words, they have one pre-designed geometry. This means that the shape of the radiator is optimized for one external temperature, and one operating condition. If radiators could change

shape while in operation, it would be possible to control the amount of radiation emitted dynamically as the spacecraft operations change.

2.2 Origami Design

Origami is the art of folding flat sheets into complex, three dimensional shapes [5]. Recently, engineering applications ranging from robotics to architecture are employing origami. Researchers are exploring ways origami can be used in the aerospace sector, including deployable structures [6,7]. Using radiators that employ deformable origami structures is one method to achieve dynamic thermal control [1]. NASA is currently researching this problem using an origami pattern known as the Muri-Ori Fold [7].

The Muri-Ori Fold is a class of fold known as a tessellation. Tessellations are fold patterns characterized by repeating patterns that are independent of sheet dimensions [8]. There are many tessellation patterns in the literature. Many of these tessellation patterns are particularly well suited for use in space-based radiators because they exhibit large cavities with wall angles that can change based on the extent to which the structure is folded (the fold percent) [1].

Researchers are also exploring methods of manufacturing origami structures and have proposed several ways to create origami shapes. The first method is to bend the patterns into the sheets using punches and wedges [9]. Another method is to affix flat metal sheets to a fabric, which would be able to flex only in areas without a plate. Finally, it may be possible to create the structure out of flat segments connected by bendable joints. While this last method is not a typical origami structure as it is not one continuous piece, it still allows for the surface topologies of interest.

5

2.3 Cavity Effect

Since these radiators are in a vacuum, the only mechanism available to transfer heat to the environment is radiation. Neither convection nor conduction can transfer the energy since these require a media, such as air or water. Radiation heat transfer is extremely sensitive to designs with surfaces that face each other due to the cavity effect. When two surfaces of a body face each other, some of the radiation emitted from one surface is absorbed by the other. Figure 2.2 illustrates this property. It shows two photons leaving the same point on the surface of the body. One photon (blue) escapes the body and carries away energy. The other photon (red) hits another face of the body and is reabsorbed. This effect is very sensitive to the angle at which the faces are relative to each other, called view factors.
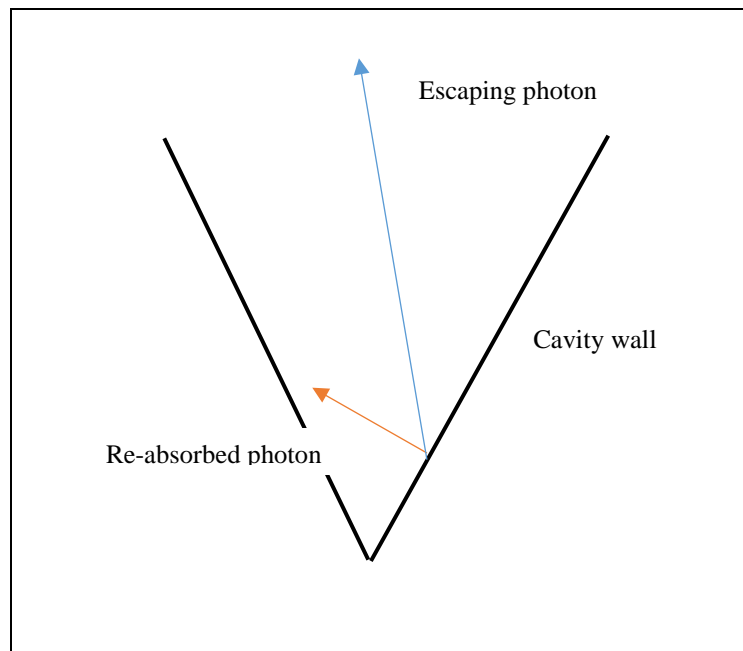
Figure 2.2 The cavity effect.

2.4 Heat Transfer

In my simulations, I assumed that all surfaces were grey surfaces: the absorption and emission coefficients are equal and wavelength independent. I also assumed that the material was

6

homogeneous throughout. Applying an energy balance equation to an isothermal, flat face (face k) of a radiator in space yields the equation:

$$q_{cond,k} + q_{rad,k} = \rho w C \frac{dT}{dt} \qquad (1)$$

where, $q_{cond,k}$ and $q_{rad,k}$ are the heat fluxes for face k from conduction and radiation transport respectively, ρ is the density of the material, w is the thickness of the element, C is the specific heat, T is the temperature of the element, and t is time. The conduction flux for face k is given by the equation:

$$q_{cond,k} = \sum_i \frac{k_s}{\Delta n_{k,i}} (T_i - T_k) \qquad (2)$$

where k_s is the thermal conductivity of the solid, $\Delta n_{k,i}$ is the distance between the center of face k and face i. The sum is conducted over all faces adjacent to face k. The radiation flux for face k is given by the equation:

$$q_{rad,k} = \varepsilon \sigma (T_{ambient}^4 - T_k^4) - \zeta \sum_{j=1}^{N} (F_{k,j} q_{out,j}) \qquad (3)$$

where ε is the emissivity of the surfae, σ is the Stefan-Boltzman constant, $\zeta = 1 - \varepsilon$, N is the number of surface faces, $q_{out,j}$ is the radiation emitted by face j (this takes the same form as the last two terms of (3)), and $F_{k,j}$ is the view factor between face k and j given by

$$F_{i,j} = \frac{1}{A_i} \int_{A_i} \int_{A_j} \frac{\cos(\Theta_i)\cos(\Theta_j)}{\pi r^2} \delta_{i,j} dA_i dA_j \qquad (4)$$

where θ is the angle of the face to the normal, r is the distance between the differential surface elements dA_i and dA_j, and $\delta_{i,j}$ is 1 if the differential surface elements can see each other (there is a ray that connects them without passing through any other surface) and 0 otherwise [10,11]. Few

analytical solutions to these equations exist, one being for a V-shaped fold pattern [1]. For more complex geometries, the finite element methods must be used.

2.5 Fluid Dynamics

Turbulent flows exhibit strong velocity fluctuations and have a high degree of chaos. Turbulent flows are very common, so much so, that even those that start as a laminar (uniform) flow can become turbulent as it progresses downstream. The Reynolds number is a ratio of internal forces to viscous forces and is an indicator of when a flow exhibits turbulent properties [12]. The Reynolds number is defined by

$$Re = \frac{\rho v d}{\mu} \tag{5}$$

where Re is the Reynolds number, ρ is the density of the fluid, μ is the dynamic viscosity, and d is the fundamental length scale for the flow; for a circular tube, d is the diameter. For internal flows, a Reynolds number greater than 2000 is considered turbulent [12].

When fluid enters a tube, the drag on the fluid causes the profile to change as it moves downstream. The fluid profile is not fully devolved until the fluid is a distance from the pipe opening, known as entrance length. The entrance length is define for laminar flow by

$$L_e = 0.06dRe \tag{6}$$

and for turbulent flow by

$$L_e = 4.4dRe^{1/6} \tag{7}$$

Equations 5 – 7 are dependent both on the geometry of the fluid wall and the viscosity of the fluid.

The working fluid used in my project was ammonia. The melting and boiling points of ammonia made it a good choice. However, other suitable materials exist. Changing the working fluid to one that has a higher viscosity, like n-propanol (19.45 x 10^{-4} Pa s vs 2.59 x 10^{-4} Pa s),

8

would lower the Reynolds number and the entrance length [13]. In other words, using n-propanol would make the flow less turbulent.

2.6 Terrestrial Applications

There may be applications for origami tubes on Earth. One possible case would be as a thermal regulator for vehicles or structures near the poles. Here, the amount of incident solar radiator varies depending on the time year. In the summer, there is direct light from the sun 24 hours a day, while in the winter, the sun is not visible at all. A deformable radiator could result in similar benefits as those possible from its use in spacecraft.

It is possible that in addition to radiation, convection is also sensitive to the topologies of the origami radiators. If flow around the tubes slows sufficiently in the areas of the cavities, then it may be possible to gain a system of dynamic control in environments that do not contain differences in radiation flux.

CHAPTER 3: GEOMETRY

I selected three tessellation patterns (Waterbomb, Huffman Waterbomb, and Huffman Stars-Triangles) because they exhibit topologies that, when folded, result in edges that overlap or are close enough to allow the edges to be joined, creating a shape that resemble a tube. Figure 3.1 shows examples of the three patterns. In Figure 3.1a, the Huffman Stars-Triangle pattern is folded to 60 percent, Figure 3.1b displays the Waterbomb pattern folded to 65 percent, and Figure 3.1c displays the Huffman Waterbomb folded to 60 percent. The plane of reflection was left in the image as a reference of the centerline.
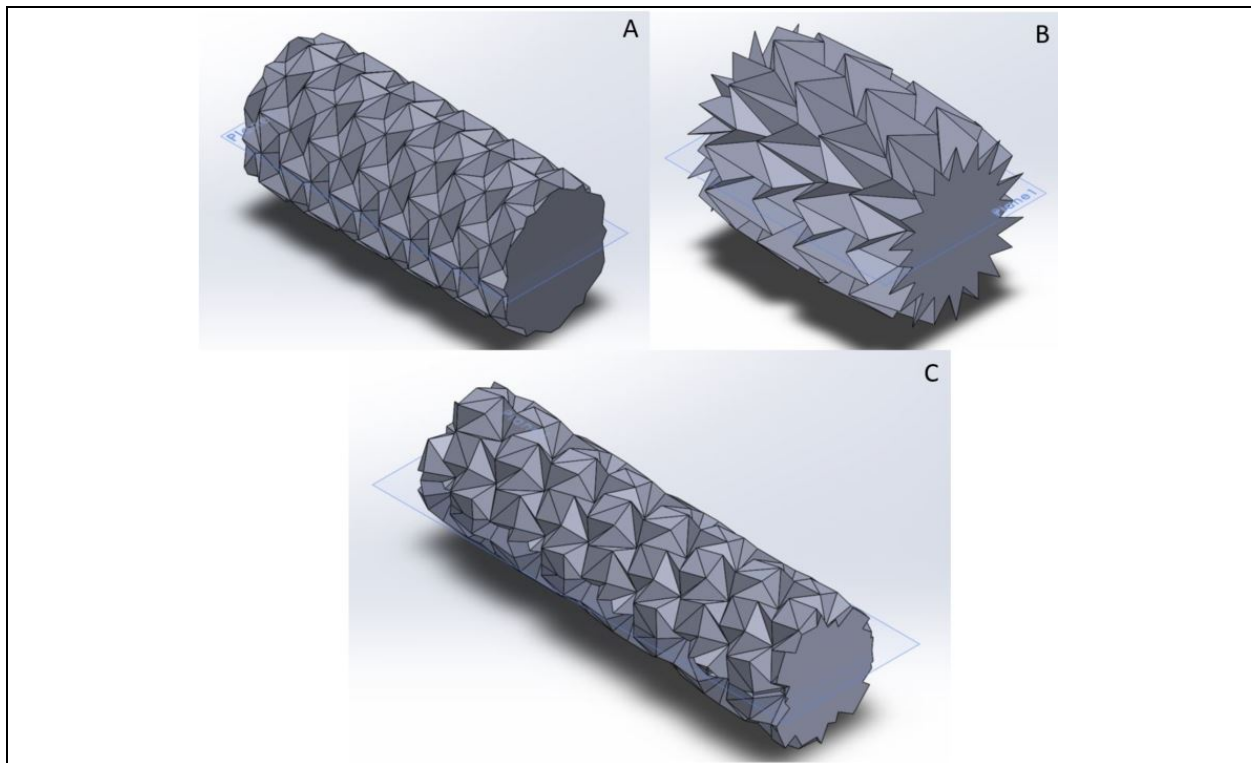
Figure 3.1 Examples of the three patterns folded. The figures were generated using Solidworks.

3.1 Creation of Surface Bodies

I created surface bodies of the three patterns using a web GL application, Origami Simulator. The program takes a pattern inlaid on a plane and folds it based on a specified fold percentage by iteratively varying the surface to minimalize the stress caused by the folds [14].

Figure 3.2 illustrates the application's outputs from folding a sheet into a tube using the Huffman Waterbomb pattern. At zero percent fold, the sheet is completely flat. As the fold percent is increase through 25 percent to 40 percent, the sheet starts to roll and takes on divots. At 50 percent fold, the sheet has completely formed into a tube.
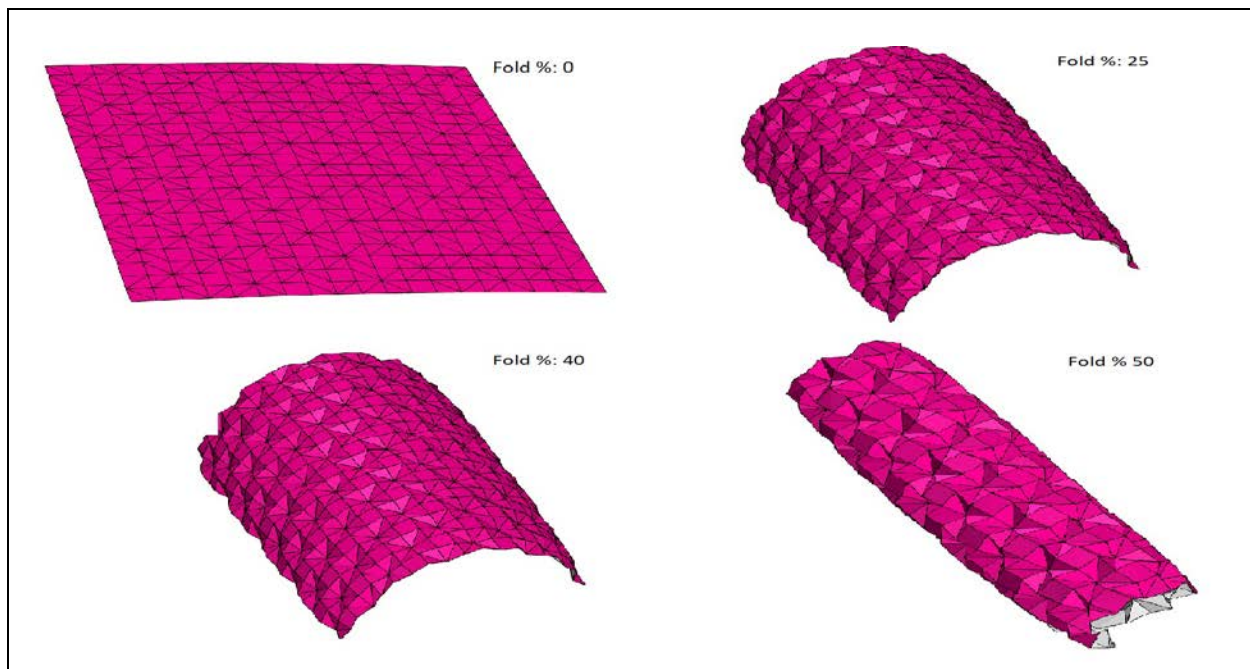
Figure 3.2 Huffman Waterbomb at difference states of being folded.

I examined each pattern using Origami Simulator, evaluating a range of fold percentages for each pattern that produced shapes where two sides of the plane either overlapped or were close enough that it was possible to join them. Once connected, these are tubes that can be used to transport the thermal fluid. I also determined intervals of fold percent for each. Table 3.1 contains the range and intervals for each pattern.

11

Table 3.1 Fold range and intervals for each pattern.

Pattern	Min Fold %	Max Fold %	Interval %
Waterbomb	61	71	2
Huffman Waterbomb	48	68	4
Huffman Stars-Triangles	48	63	3

For the Waterbomb pattern, I found the minimum and maximum useable fold percentages to be 61 percent and 71 percent, respectively. I decided to run simulations at two percent intervals to give six configurations I would test. Likewise, for the Huffman Waterbomb pattern, I found the minimum useable fold percentage was 48 percent, the maximum useable fold percentage was 68 percent, and the sampling interval was four percent. These parameters produced five configurations. I examined the Huffman Stars-Triangles pattern to determine a minimum useable fold percent of 48 percent, a maximum useable fold percent of 63 percent, and a sampling interval of three percent. These parameters made six configurations.

I exported the surface bodies as stereolithographic files, or stl files. Many of the configurations contained regions where the surface body overlapped. Since the Origami Simulator is unable to account for overlap, I simplified the model by removing the overlapping areas when I created the solid body.

3.2 Creation of Solid Bodies

Initially, I loaded the stl files generated by Origami Simulator to Meshmixer, a program designed to be work with surface bodies. However, because Solidworks showed a much greater capacity to work with surface bodies, I opted to use Solidworks to convert to solid bodies. Figure 3.3 shows the stages of a surface body being converted into a solid body.

12
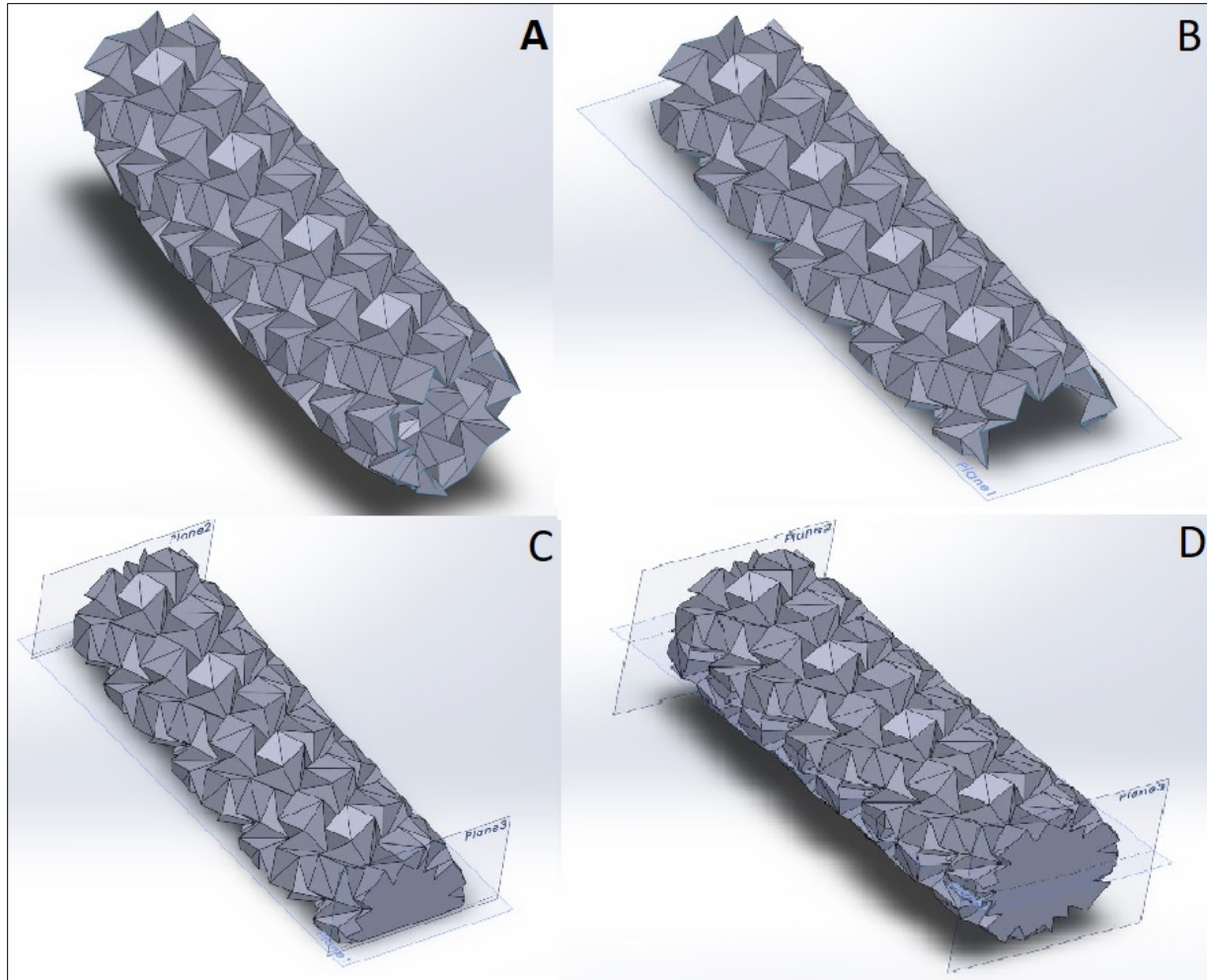
Figure 3.3 Stages of using Solidworks to create a solid body from a surface body. The Huffman Waterbomb pattern is used as an example.

Figure 3.3a shows the imported surface body. Using the 'surface trim' function, as well as a reference plane, I removed all the overlapping elements and sliced the surface bodies along the long axis (Figure 3.3b). Most of the instances were not cut directly in half because they exhibited small, sharp edges and close vertexes, making meshing difficult. Afterwards, two reference planes were placed perpendicular to the axis and at the ends of the tube to create planar inlets and outlets for the FLUENT module. I used the 'intersect' feature to create a solid body from all three planes and the trimmed surface body (Figure 3.3c). In many cases, if the three planes were positioned close to or on vertices or sharp edges, the program was unable to intersect

13

the regions. To correct for this, I had to adjust the positions of the reference planes. This introduced some error in my models. I used the 'mirror' function to reflect the design across the long plane (Figure 3.3c). Finally, I scaled the model so that all instances had approximately the same transverse length, so the models could be compared more equitably.

3.3 Geometry Dimensions

Each instance of the solid geometries had slightly different dimensions due to my using the mirror operation, setting perpendicular planes for the inlets and outlets, and using the scale operation to get a consistent transverse length. Figure 3.4 shows an example geometry. In this figure, L is the transverse length, D is the outermost diameter, and A is the area of the fluid wall. A table of the dimensions for each instance of solid model is included in Appendix A.
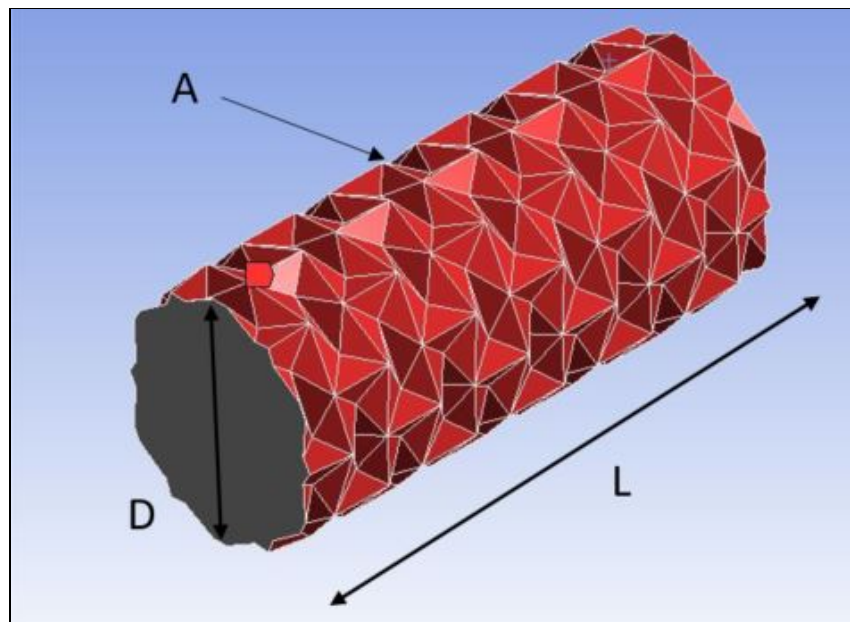
Figure 3.4 Solid model with dimensions labeled. The Huffman
Stars-Triangles is used as the example.

CHAPTER 4: MESHING

Once I created the solid bodies, I imported them into the Geometry module of ANSYS Workbench 18.1. I used ANSYS Mechanical to generate meshes for each body. I then selected the Waterbomb pattern at 71 percent fold and conducted a mesh study of one of its geometries to determine if different element numbers would yield different results. After, I meshed each solid body as described below.

4.1 Mesh Study

I analyzed the mesh to determine if the number of elements had any effect on the solution. This mesh study invloved selecting the Waterbomb pattern at 71 percent fold and meshing the body five times, varing the mesh options. I imported each mesh into ANSYS FLUENT and ran under the same options that are discussed in Chapter 5.

Table 4.1 Statistics from mesh study.

Number of Elements	Max Skewness	Radiation Flux (W)	Percent Difference from ABS Max
105670	0.961	-0.01592419	1.535932093
205479	0.93	-0.01617259	0
210214	0.94	-0.01576689	2.508565418
275911	0.938	-0.01558731	3.618962702
412594	0.945	-0.01566087	3.164119043
ABS Max Flux (W): 0.01617259		**Difference:** 0.00058528	
ABS Min Flux (W): 0.01558731		**Percent Difference From Max:** 3.618962702	
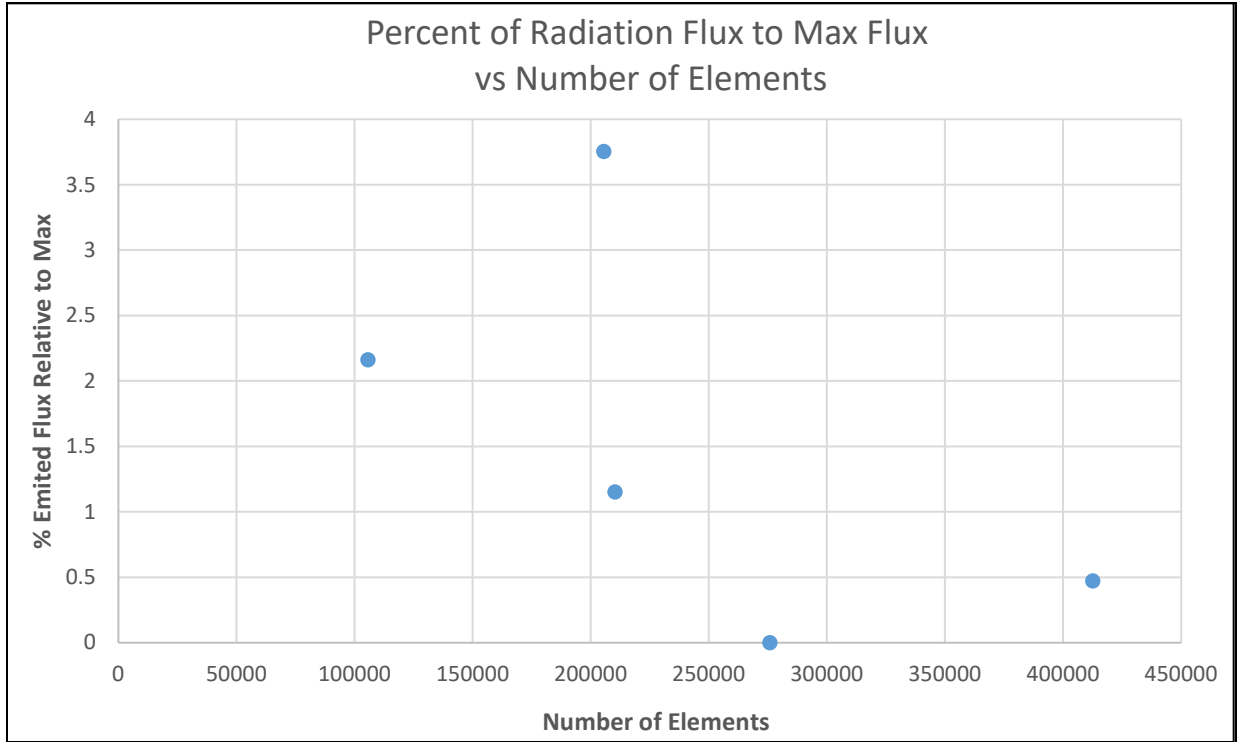
Figure 4.1 Percent of radiation flux to max flux vs number of elements.

Table 4.1 contains the statistics from the mesh study. The first column of Table 4.1 lists the number of elements used in each simulation. The second contains the maximum element skewness. The third shows the net amount of energy in the form of radiation through the Fluid Wall (described in Chapter 5) calculated during the simulation. The negative sign on the results indicates that the body was emitting energy. The last column shows the percent difference from the maximum absolute value of radiation flux. This is calculated with the equation below:

$$Percent\ Difference\ From\ ABS\ Max\ =\ 100 * \frac{(|F_R| - max|F_R|)}{max|F_R|} \qquad (8)$$

where, F_R is the flux from radiation. The bottom of Table 4.1 lists the maximum and minimum values of the absolute value of the fluxes and the difference between the two. The maximum percent difference from maximum is also listed. Figure 4.1 plots the percent difference from maximum against the number elements.

16

Table 4.1 and Figure 4.1 show as the number of mesh elements was increased from 105670 to 210214, the radiation flux only changed by 0.00016 W. The small change in flux when the element number was nearly doubled was enough to demonstrate mesh independence. However, the data also showed the maximum difference was only .00058528 W, or 3.16 percent, when all the meshes were examined, confirming the solution was independent of the mesh chosen. Even when the element number was increased to 412594, the solution varied by less than 3.16 percent.

4.2 Meshing of Solid Bodies

Based on the results of the mesh study, I decided all bodies must be meshed with at least 100,000 elements. Also, I meshed each body so the maximum element skewness was less than 0.95 because elements skewned more than 0.95 led to errors and issues with convergence, and should therefore, be considdered unacceptable [15]. The exception was the Waterbomb pattern at 61 percent fold; I was unable to find a mesh that gave a max skewness lower than 0.95.

Some issues arose as the solid bodies have sharp edges at the surfaces and at virtices that are close together; this caused the mesh to take on high skew values near these zones. To achieve the desired mesh properties, I refined the mesh from default by using the adaptive size control, using the curvature size control, and creating spheres of influence to locally reduce mesh size.

Since the geometry of each of the bodies was different, I meshed each body with different options. The exact method of each mesh is not included in this text, but a full list of mesh statistics is included in Appendix B. Figure 4.2 shows an example mesh with the coloring set to show element skewness. The higher skewed elements are the on the outermost edges close to the virtexes of the fold. The max skewness was 0.88331, the min skewness was 2.9317×10^{-4}, the

17

average was 0.24889, and the standard deviation was 0.13639. Figure 4.3 shows a histrogram of

the skewness elements.
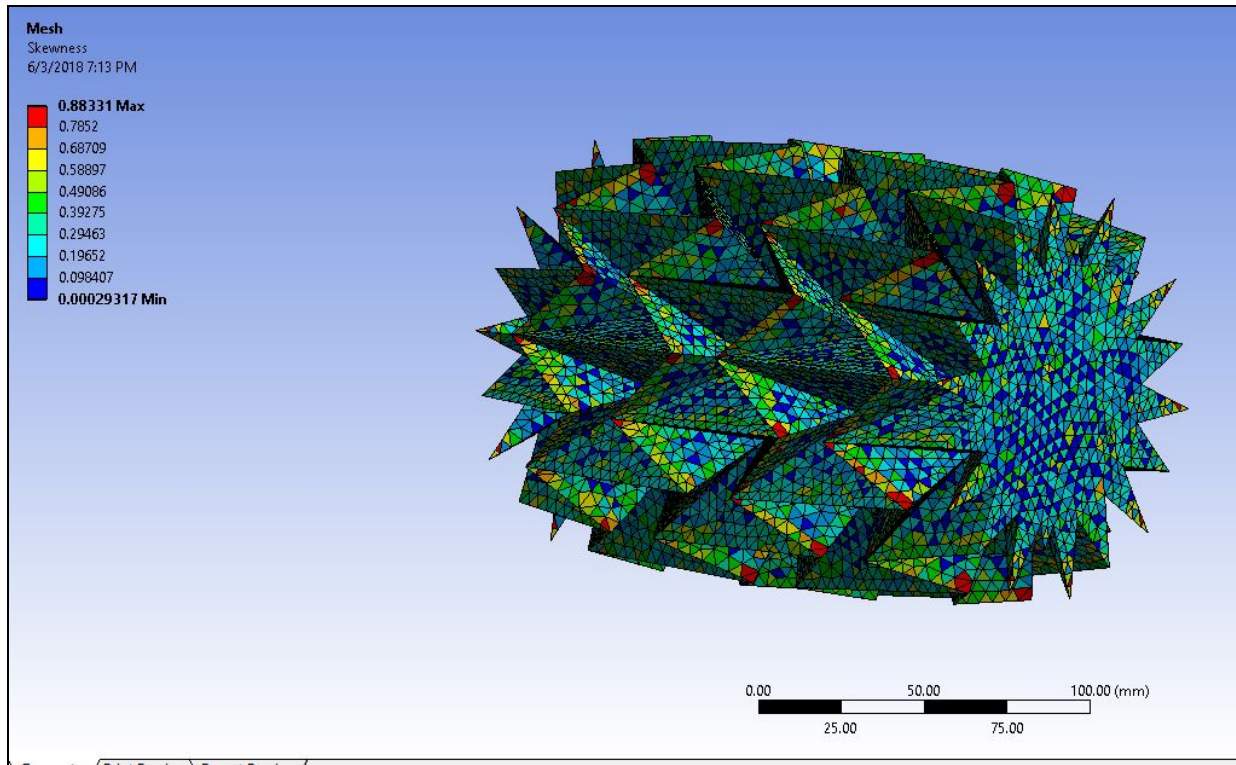
Figure 4.2 Mesh of Waterbomb pattern at 67 % fold. Color graph shows element skewness.
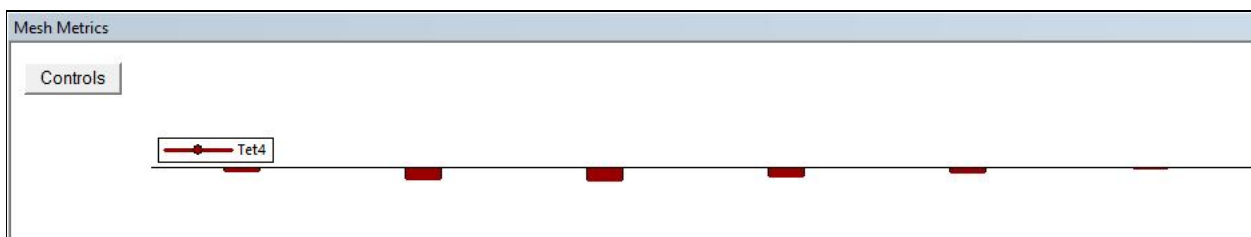
Figure 4.3 Histogram of skewness for elements in the Waterbomb pattern at 67 % fold.

18

CHAPTER 5: FLUENT METHODS

I used ANSYS FLUENT, an industry standard computational fluid dynamics solver, to set up the physics of the problem and to solve the governing equations. I used CFD Post, another module in ANSYS Workbench, to create contour and vector plots of the solutions.

5.1 Name Selection

The first step in simulating the problem was to add distinct names to each of the zones of the solid model to allow the FLUENT solver to initialize the problem and to assist the program's user navigate the interface. I set the name selections in ANSYS Mechanical. Figure 5.1 shows an example solid model with labels of the names of each surface zone.
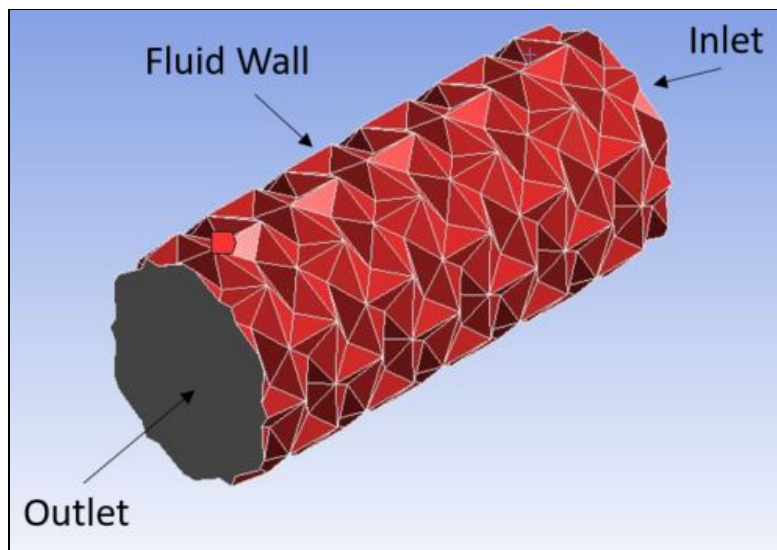
Figure 5.1 Diagram showing surface name selections.
Huffman Stars-Triangles is used as the example.

The Inlet, where fluid will enter the solution region, is parallel with the Outlet, but it is not displayed in this figure. The Outlet is the area through which the fluid will leave the solution region. The remaining faces that bound the fluid domain are named the Fluid Wall; this is the

19

area highlighted in red. The body name selection Fluid Body is not pictured. However, Fluid

Body is the region of the fluid domain.

5.2 FLUENT Settings

FLEUNT has numerous settings and a complete list of all of them is not feaseable. All

default settings are listed in the FLUENT User Guide. However, I present all the fields that I

changed. Assume I left the default value for any setting not mentioned.

5.2.1 Setup

This section outlines the options and fields I changed in the Setup block of the FLUENT

interface and the reasons for my selections. Figure 5.2 lists the FLUENT settings that were

modified.


```
Models:
    • Energy Equation: set to be active
    • Viscous Model: set to k-epsilon
        o k-epsilon Model: set to Realizable
        o Near-Wall Treatment: set to Scaleable Wall Functions
    • Radiation: set to Surface-to-Surface (S2S)
        o View Factors were calculated
Materials:
    • Fluid: added ammonia-liquid from FLUENT database
Cell Zone Conditions:
    • Fluid Body: set Material name to ammonia-liquid
Boundary Conditions:
    • Fluid Wall:
        o Thermal:
            ▪ set Thermal Conditions to Radiation
            ▪ set External Radiation Temperature (K) – value changes
            ▪ set Shell Conduction to be active. – set Thickness (m) to 0.001
    • Inlet:
        o Momentum:
            ▪ set Velocity Magnitude (m/s) to 0.2
        o Thermal:
            ▪ set Temperature (K) to 276
Solution:
    • Monitors
        o Residual
            ▪ set Absolutre Criteria for continuity to 0.01
    • Initalization Methods: use Hybrid Initalization
    • Run Calculation: set Number of Iterations to 250
```

Figure 5.2 List of FLUENT settings modified

20

Because the flow of energy through the fluid and between the walls and enviorment was the main intrest of the simulations, I set the energy equation to active. I selected the k-epsilon model because it is excellent at modeling fluid flow with turbulence when the pressure difference between the Inlet and Outlet is low [11]. In the simulation, the difference is zero. I selected the Surface-to Surface (S2S) model because it works by calculating the flux between surfaces, taking into account orientation and distance. The S2S model is recommended for simulations involving spacecraft [11]. The S2S model does not work with symmetry boundray conditions because the model needs each surface to calculate the view factors [11].

I used the ammonia-liquid material because it is the working fluid currently used in the Internaional Space Station (ISS) thermal mangement system [4]. I set the thermal boundary conditions on the walls to radiation because my model assumed the radiator is in the vacuum of space where convection and conduction are not available since there is no media to mediate the transfer of energy, meaning the only means of heat transfer is radiation. I selected temperature as the independent variable. It ranged in value from 173 K to 394 K, depending on whether the model was in direct sunlight or the shadow of the Earth. I selected 173 K as the lower boundray for my simulations because it is 20 K lower than the melting point of the working fluid, ammonia [13]. I activated the Shell Conduction model because it simulates a sheet around the Fluid Wall by adding an extra layer of mesh to the outside of the Fluid Wall and then applying the boundary conditions to the outside of this new surface. Conduction occurs inside this shell [11]. I selected the thickness of the shell to be 0.001 m and the material to be aluminum. I chose the velocity at the inlet as 0.2 m/s so the fluid would pass through the tubes with enough time to exchange energy. I set the temperature of the inlet to 276 K because this is the working temperture of the current system on the ISS [4].

21

5.2.2 Monitors and Residuals

FLUENT plots the residuals at each iteration step. Figure 5.2 is a plot of the redisuals for the Waterbomb pattern at 71 percent fold.
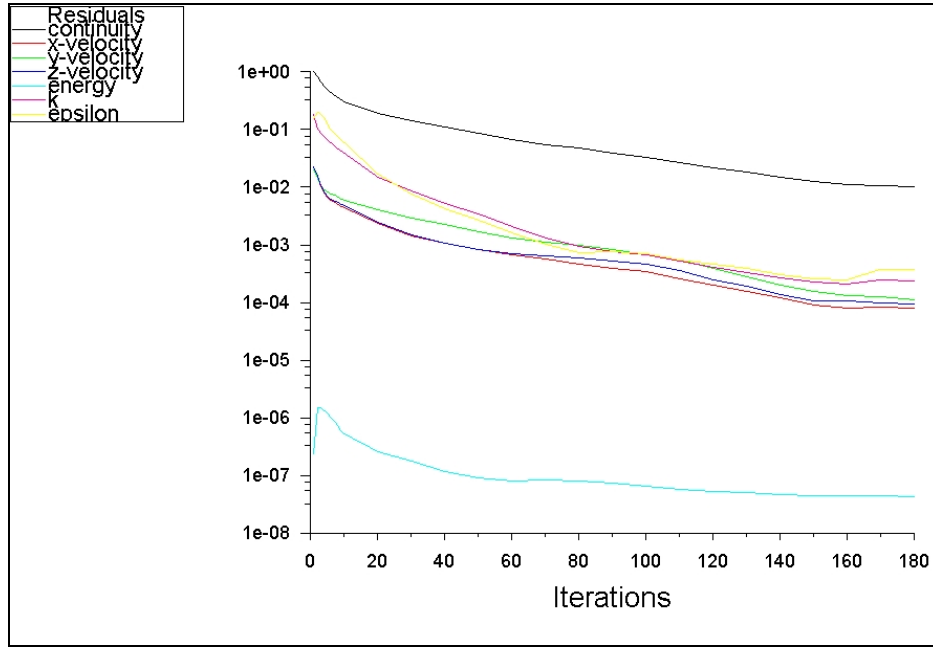
Figure 5.3 Plot of the residuals for Waterbomb pattern at 71 % fold.

The continuity residual was the largest, ending between 0.01 and 0.1. The x-velocity, y-velocity, z-velocity, k, and epsilon residuals were grouped together and ended near 0.001. The energy residual was the lowest, ending near 1×10^{-7}. Residual plots from all the simulations showed a similar monotomic decreasing form. The number of iterations to reach convergence changed based on boundary conditions. Since energy, the quantity of interest, quickly reached a residual value six orders of magnitude smaller than the continuity, I loosened the continuity convergence requirement to .01. I left all the others at .001. I set the iteration value to 250 to constrain the computational time. All the the simulations finished before they reached the iteration value.

22

CHAPTER 6: RESULTS

My goal was to study how changing fold percentages on each of the three patterns affected the amount of energy released or absorbed through the fluid walls. I plotted the velocity flow through each body, the temperature distribution of the fluid wall, and the distribution of emitted radiation at the fluid wall. Finally, I created plots of the total radiation flux through the Fluid Wall as a function of fold percent and ambient temperature.

6.1 Fluid Profiles

While the radiation flux through the Fluid Wall was my principle interest, the flow profile through the origami tubes was also important because the fluid carries heat to or away from the inside surfaces of the walls.

I calculated the Reynolds number and the entrance length each of the solid bodies, assuming ammonia as the working fluid. The density of ammonia is 683.2 kg/m^3, and the viscosity is 2.59 x 10^{-4} [13]. The results are listed in Appendix C. For all the solid bodies, the Reynolds number was on the order of 1 x 10^4. This means that all the flows were highly turbulent. I also found the entrance lengths to be an order of magnitude greater than the length of the solid bodies. This means the flow was not fully developed in any part of the pipe. This can be seen in all the velocity profile figures.

Figure 6.1 shows the centerline velocity contour plots for the Waterbomb pattern with the temperature held constant at 173 K but at various fold percent.

23
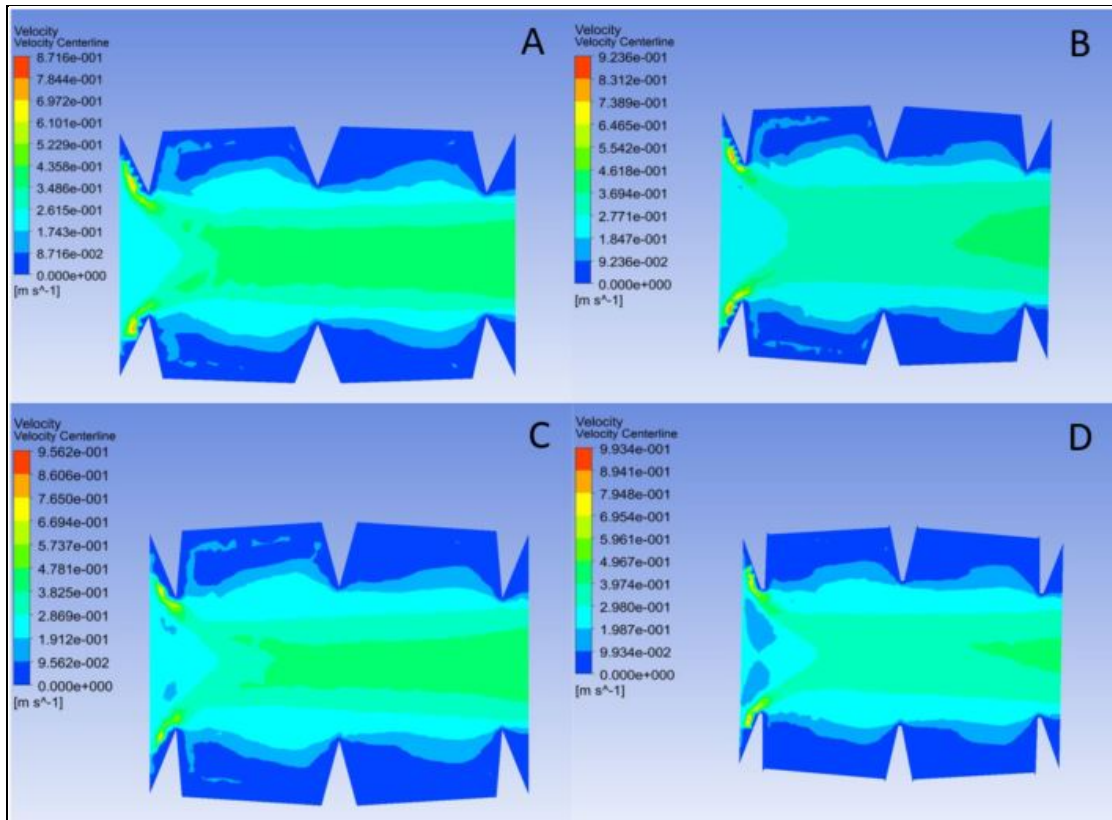
Figure 6.1 Velocity contour plots for the Waterbomb pattern at 173 K. A is at 61 % fold, B is at 65 % fold, C is at 67 % fold and D is at 71 % fold.

Figure 6.1a has the fold percent set at 61 percent. Figure 6.1b has the fold set at 65 percent. Figure 6.1c is set at 67 percent, and Figure 6.1d is set at 71 percent. In all cases, the inlet is on the left and the outlet is on the right. All four plots showed similar flow profiles. There was a fast-moving flow at the center, which slowed as the flow approached the walls. There was also a section of quickly-moving fluid near the walls of the inlet caused by a uniform incoming velocity accelerating as the diameter of the flow area decreased. The flow in the areas of the 'fins' (the areas between the peaks and troughs of the folds) was particularly interesting. Although it appeared that there was no moving fluid there, this was not the case. Figure 6.2 is a vector plot of the velocity for the same geometries as in Figure 6.1.

24

Figure 6.2 Velocity vector plots for the Waterbomb pattern at 173 K. A is at 61 % fold, B is at 65 % fold, C is at 67 % fold and D is at 71 % fold.

Figure 6.2 shows, for all the geometries, there is circulation in the fin areas, but its velocity is significantly less than that of the fast-moving fluid near the walls of the inlet.

Since the flow is three dimensional, I created a vector plot of velocity for the entire fluid body. This is displayed in Figure 6.3 for the Waterbomb pattern at 61 percent fold at 173 K. Since this plot is crowded, little can be determined. However, two features that can be seen are: 1) as expected, the flow was three dimensional, and 2) there were large changes of directions near the corners of the body, indicated by large vectors, caused by elements with high skewness.

25
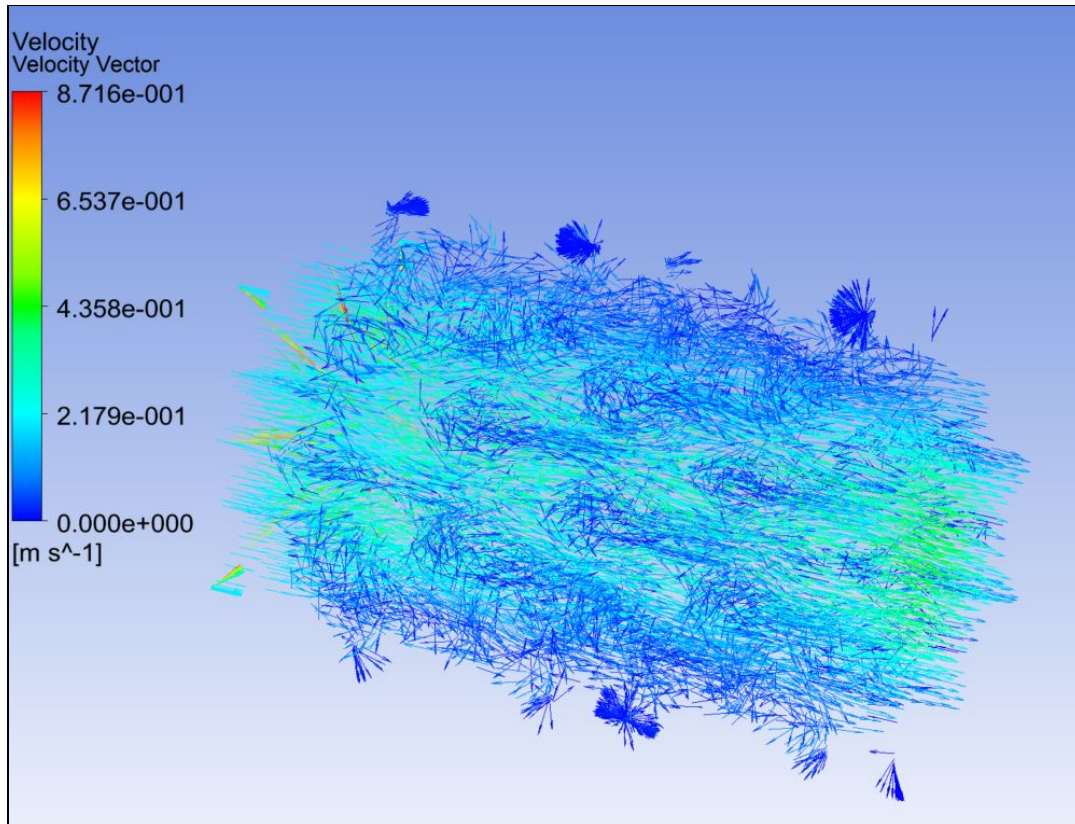
Figure 6.3 Velocity vector plot for the Waterbomb pattern at 61 % fold and 173 K.

To investigate the effect of the ambient temperature imposed, I plotted the velocity contours for the Waterbomb Pattern at 61 percent fold at various ambient temperatures. Figure 6.4 displays the results. There is no discernable difference between the plots. Thus, external temperatures had no effect on the fluid flow.

I also created vector plots of centerline for the Huffman Waterbomb and Huffman Stars-Triangles at varying fold percent. Figure 6.5 and Figure 6.6 display the results. There were minute differences in the flow fields when moving between fold percent for both the Huffman Waterbomb and the Huffman Stars-Triangles patterns. However, the bulk flow remained the same: linear, quickly moving fluid in the center, with slow moving fluid circulating in the fins. I determined these differences to be unimportant. There was no appreciable difference in the radiation flux profiles (discussed in Chapter 7) over the different geometries.

26
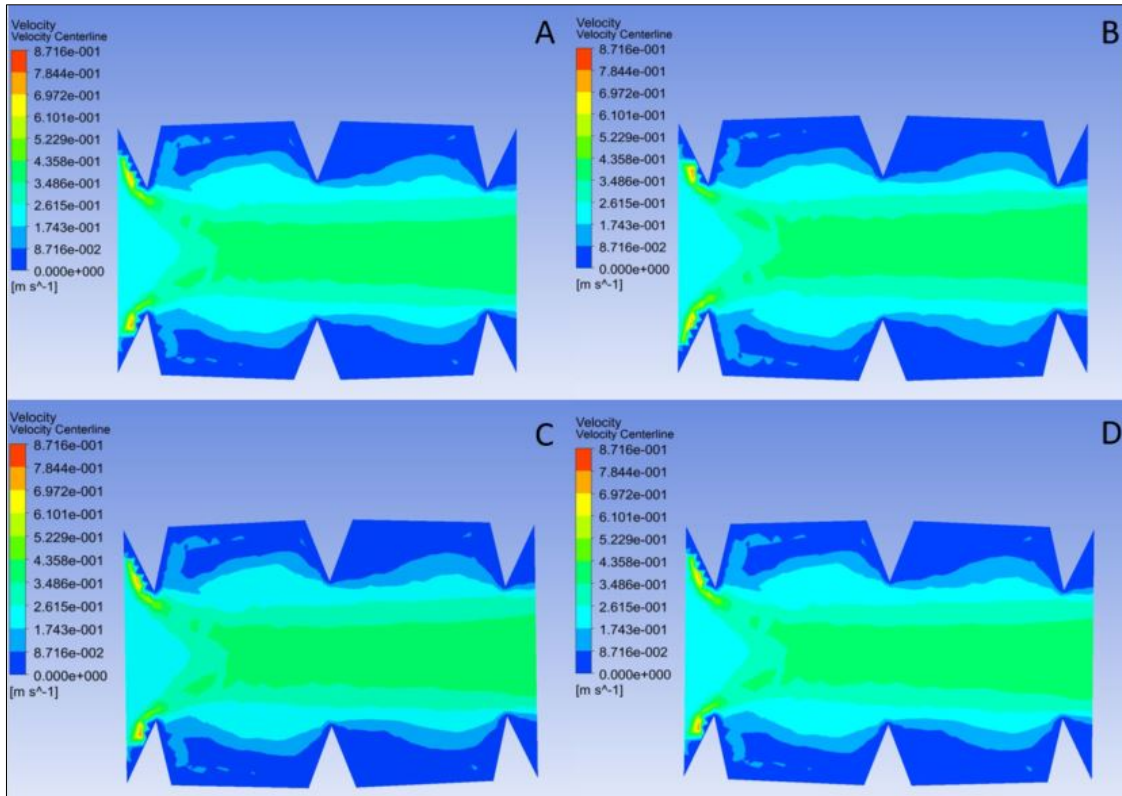
Figure 6.4 Velocity contour plots for the Waterbomb pattern at 61 % fold. A is at 173 K, B is at 174 K, C is at 314 K, and D is at 394 K.
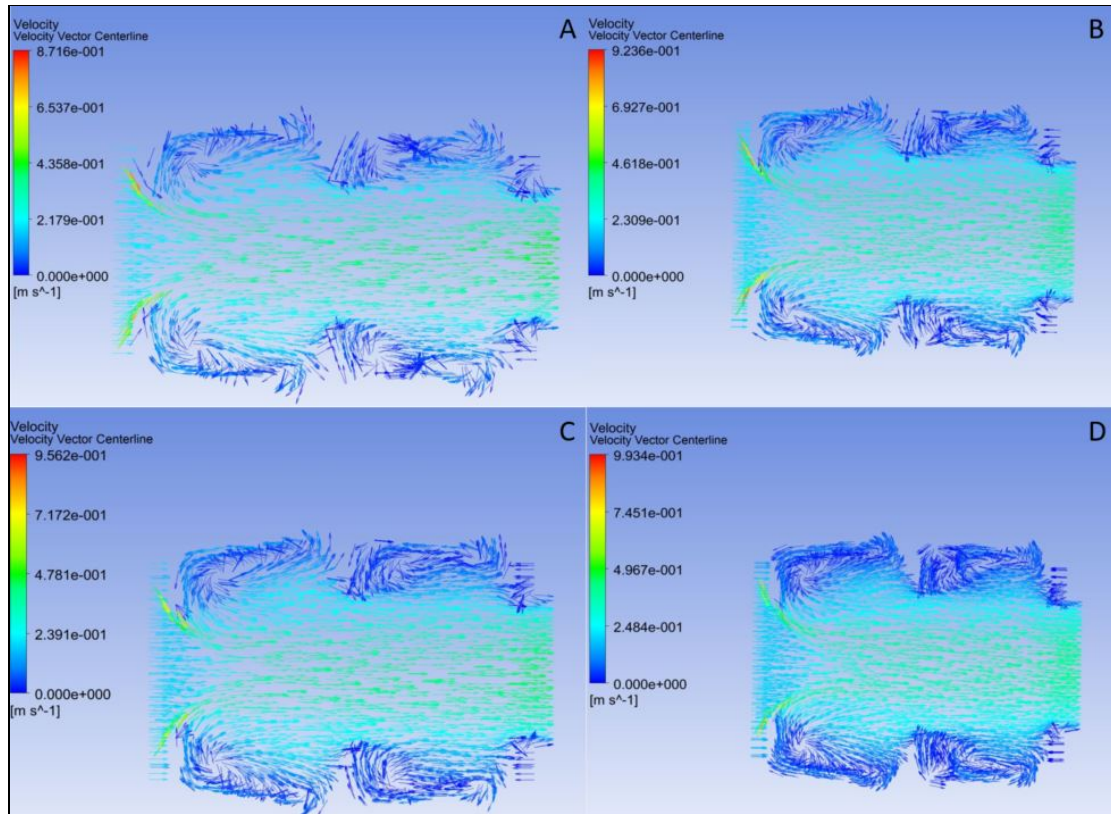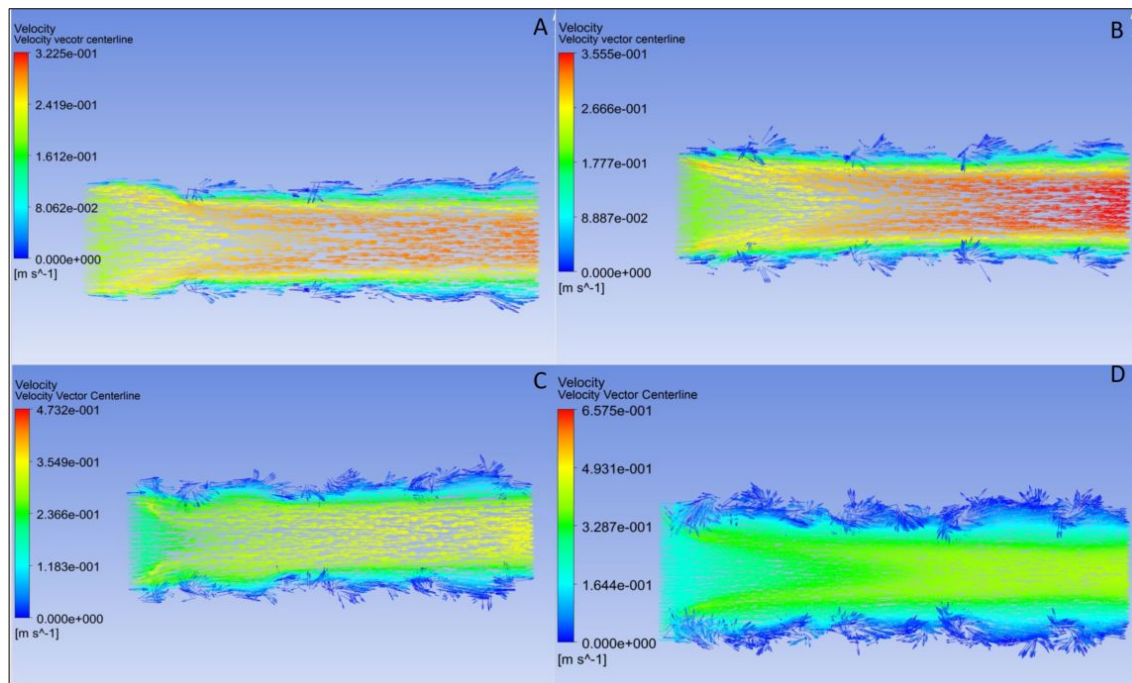

Figure 6.5 Velocity vector plots for the Huffman Waterbomb pattern at 173 K. A is at 48 % fold, B is at 56 % fold, C is at 64 % fold and D is at 68 % fold

27
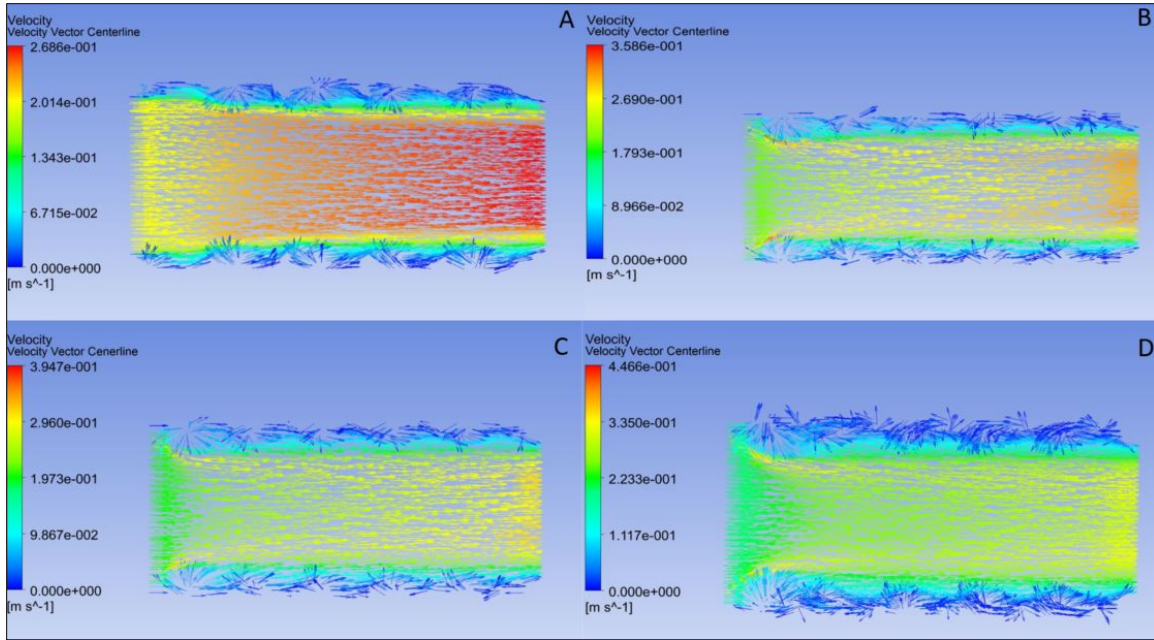
Figure 6.6 Velocity vector plots for the Huffman Stars-Triangles pattern at 173 K. A is at 48 % fold, B is at 54 % fold, C is at 57 % fold and D is at 63 % fold.

6.2 Temperature and Radiation Profiles

To examine the thermal properties of the solutions, I created temperature and radiation flux contour plots. Figure 6.7 is a plot of the radiation flux through the fluid wall, the temperature of the fluid wall, and the centerline temperature for the Waterbomb pattern at 61 percent fold with ambient temperature set to 173 K.

Figure 6.7 shows several important characteristics of the physics of the problem. First, the temperature on the second set of fins was lower than that on the first set because there was less fluid circulation in these regions. This pattern would continue if the model was extended, with each subsequent fin having less fluid circulation. Second, the wall surfaces far from the center of the flow had a gradual temperature gradient, while the surfaces close to the fluid center had a sharp temperature change. Third, areas of high emitted radiation corresponded directly with those of high temperatures, confirming the radiation model is functioning properly. Finally, temperature in the cavities of the fluid wall was higher than at the peaks, and this effect was

independent of the thickness of the boundary layer around the surface caused by both the cavity effect and conduction in the aluminum shell. I could not determine clearly which mechanism was dominant.

Figure 6.7 Thermal contour plots for Waterbomb pattern at 61 % fold at 173 K. A is the radiation flux through the fluid wall, B is the temperature on the fluid wall, and C is the centerline temperature.

Figure 6.8 and Figure 6.9 plot the same thermal properties for the Waterbomb pattern at 61 percent fold at 274 K and 394 K respectively. These plots showed the same qualitative data as in the case at 173 K ambient temperature. At 394 K ambient temperature, the tube was absorbing energy from the environment, and this caused the color plot inversion. As in the case of the fluid flow, a change in temperature had little effect on the temperature profiles.

29

Figure 6.8 Thermal contour plots for Waterbomb pattern at 61 % fold at 274
K. A is the radiation flux through the fluid wall, B is the temperature on the
fluid wall, and C is the centerline temperature.

Figure 6.9 Thermal contour plots for Waterbomb pattern at 61% fold at 394
K. A is the radiation flux through the fluid wall, B is the temperature on the
fluid wall, and C is the centerline temperature.

Figures 6.10 and 6.11 are contour plots of the same thermal properties as those in Figure 6.7 but for the Waterbomb pattern at 67 percent fold and 71 percent fold and subjected to a 173 K ambient temperature.

Figure 6.10 Thermal contour plots for Waterbomb pattern at 67 % fold at 173 K. A is the radiation flux through the fluid wall, B is the temperature on the fluid wall, and C is the centerline temperature.
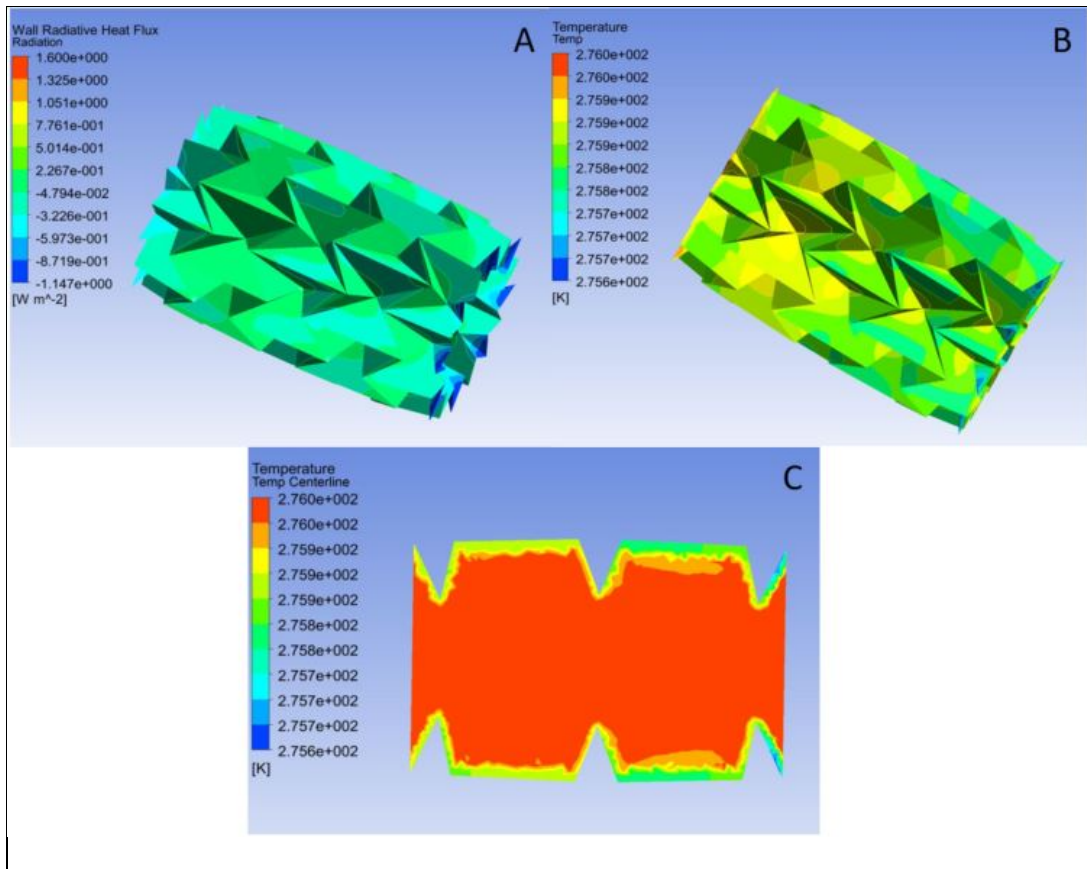
Figure 6.11 Thermal contour plots for Waterbomb pattern at 71 % fold at
173 K. A is the radiation flux through the fluid wall, B is the temperature
on the fluid wall, and C is the centerline temperature.

Figure 6.10 and Figure 6.11 are similar. Both show a larger boundary region next to the

fluid walls when compared to Figure 6.7. Both also have a larger boundary region in the second

set of fins as compaired to the first, again caused by lower circulation in these regions. Lastly,

both show higher temperatures and radiation fluxes in the center of the cavities. This is

especially true of the Waterbomb pattern at 71 percent fold because its cavity openings are

smaller than those of the other two models.

Figure 6.12, Figure 6.13, and Figure 6.14 are plots of the thermal properties for the

Huffman Waterbomb pattern folded at 48 percent, 64 percent, and 68 percent respectivly.

Ambient temperature is set at 173 K for all three plots.

32

Figure 6.12 Thermal contour plots for Huffman Waterbomb pattern at 48 % fold at 173 K. A is the radiation flux through the fluid wall, B is the temperature on the fluid wall, and C is the centerline temperature.

Figure 6.13 Thermal contour plots for Huffman Waterbomb pattern at 64 % fold at 173 K. A is the radiation flux through the fluid wall, B is the temperature on the fluid wall, and C is the centerline temperature.
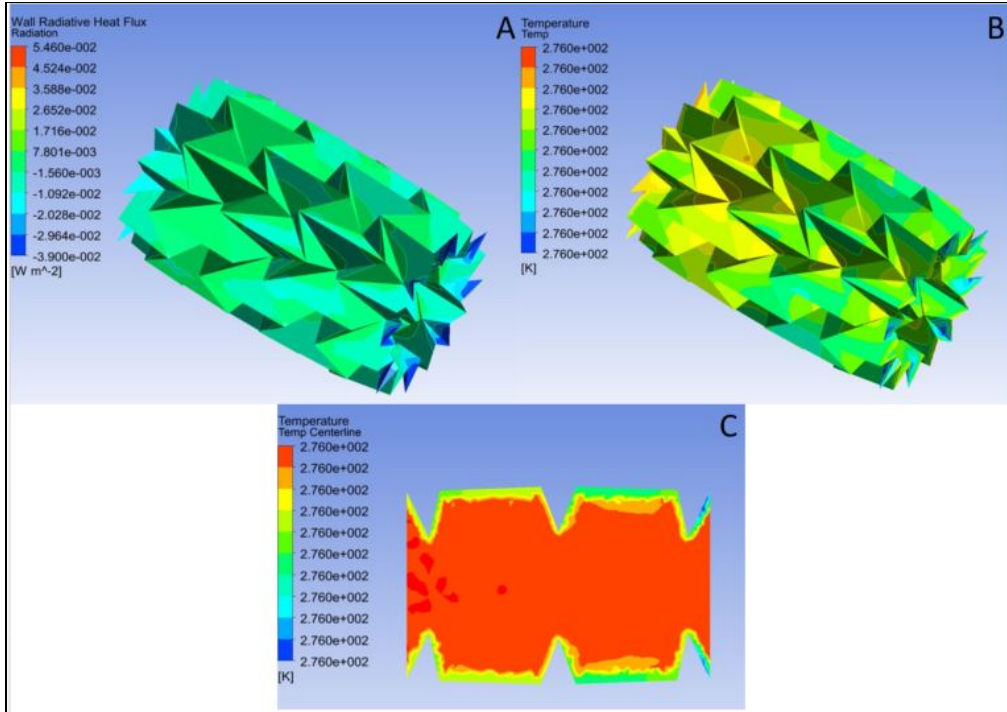
33

Figure 6.14 Thermal contour plots for Huffman Waterbomb pattern at 68 % fold at 173 K. A is the radiation flux through the fluid wall, B is the temperature on the fluid wall, and C is the centerline temperature.
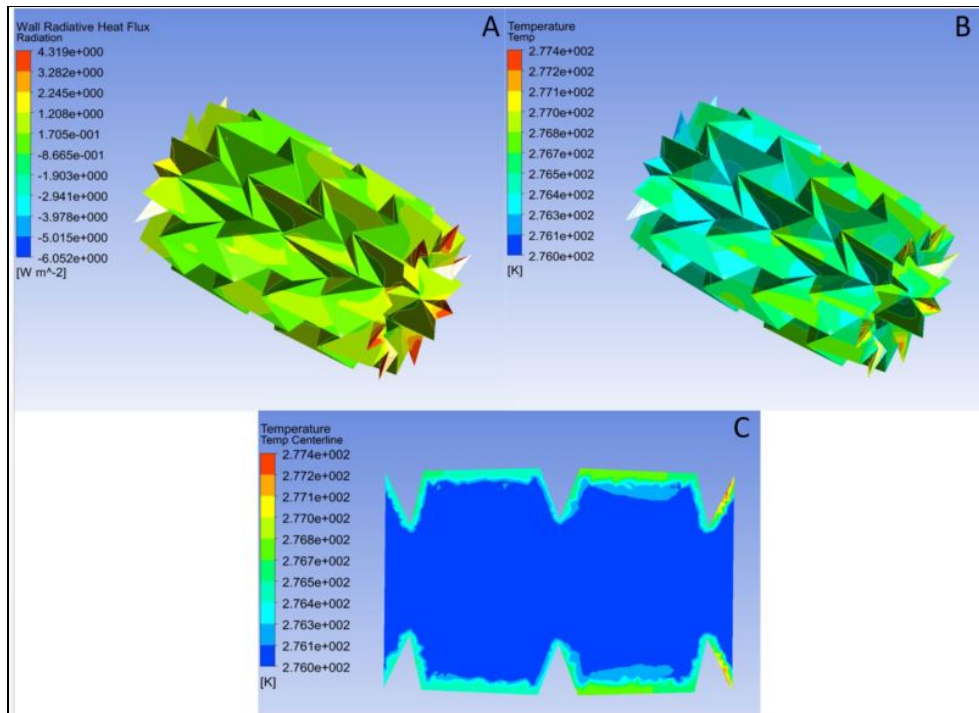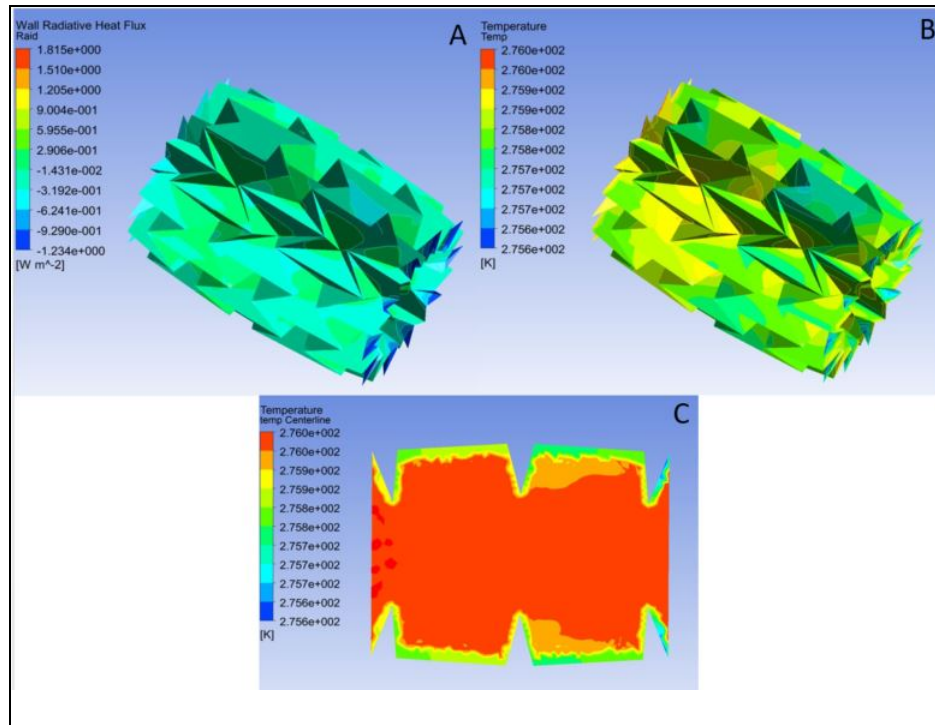
Examining the centerline temperature plots for the three figures, it was clear that as the fluid moves through the tube, the boundary layer close to the outcroping folds became thicker. This effect became more pronounced as the fold pattern increased from 48 percent to 68 percent. Examining the fluid wall temperature plots, I found the boundary layer was the dominating effect. Close to the inlet, the boundary layer was thin and the fluid wall increased in temperature. At a point, a thick boundary layer formed in the fins and insulated the fluid wall from the center flow, allowing it to remain cooler. This effect contined and became more pronounced closer to the outlet. Intrestingly, there was not an exact correlation between emitted radiation and surface temperature. The emited radiation was more uniform throughout the fluid wall.

Figure 6.15, Figure 6.16, and Figure 6.17 are are plots of the thermal properties for the Huffman Waterbomb pattern folded at 48 percent, 54 percent, and 63 percent respectivly. Ambient temperature is set at 173 K for all three plots.

34
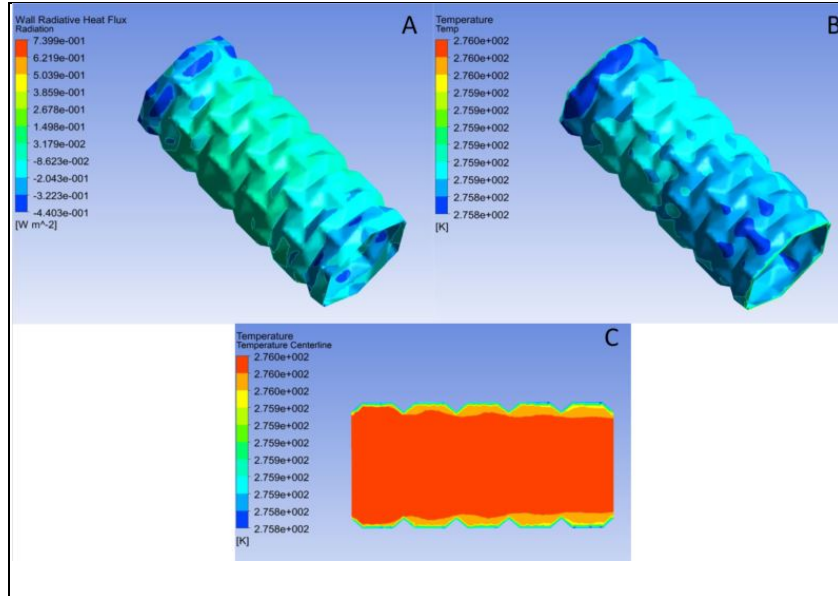
Figure 6.15 Thermal contour plots for Huffman Stars-Triangles pattern at 48 % fold at 173 K. A is the radiation flux through the fluid wall, B is the temperature on the fluid wall, and C is the centerline temperature.
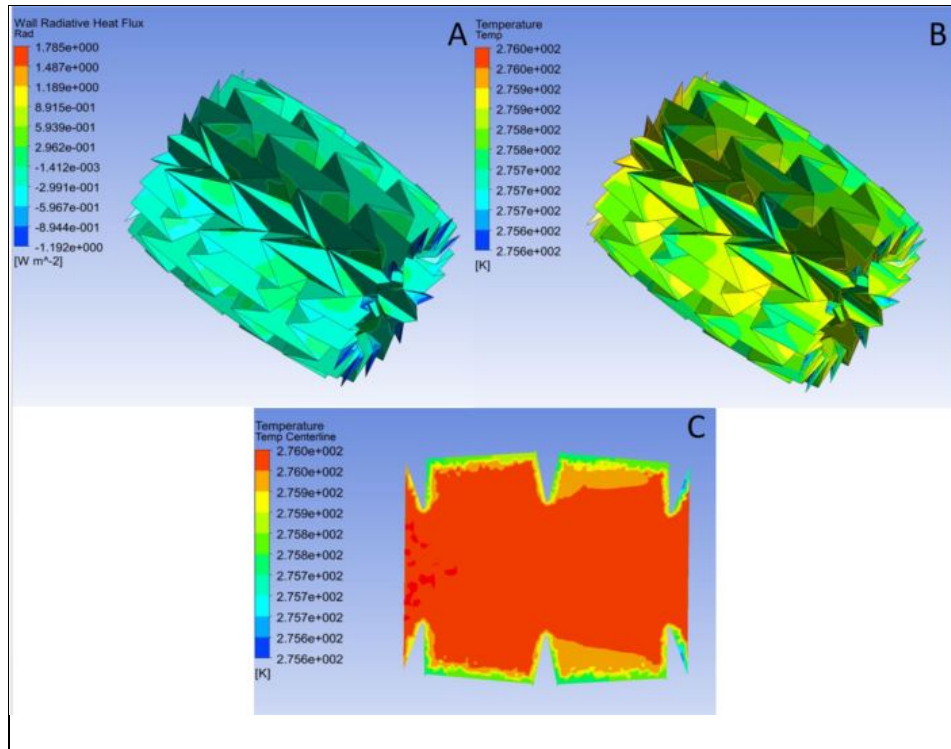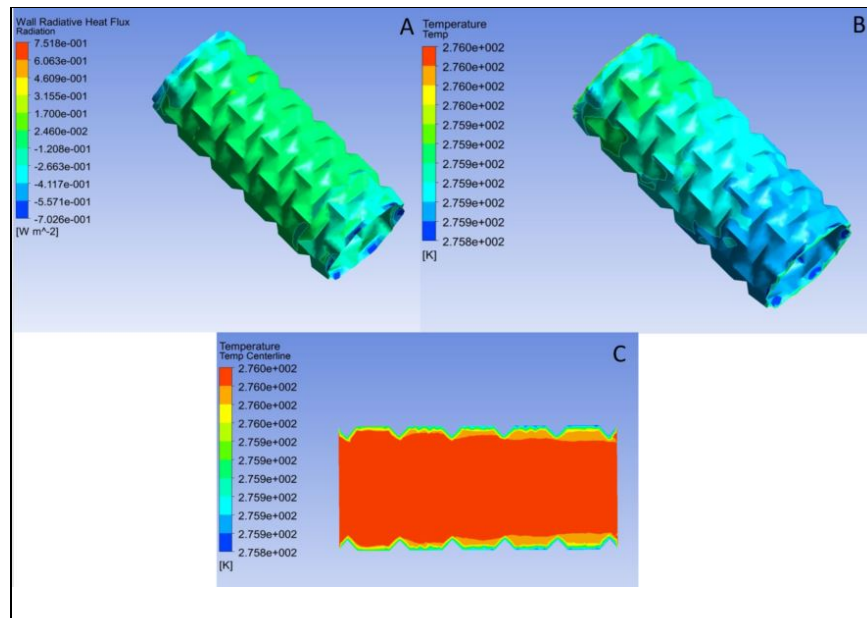

Figure 6.16 Thermal contour plots for Huffman Stars-Triangles pattern at 54 % fold at 173 K. A is the radiation flux through the fluid wall, B is the temperature on the fluid wall, and C is the centerline temperature.
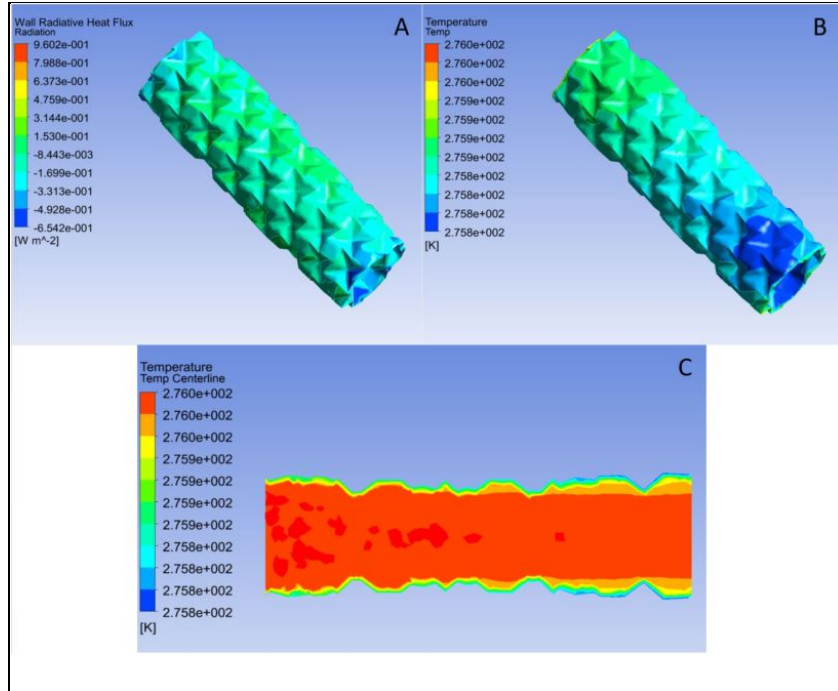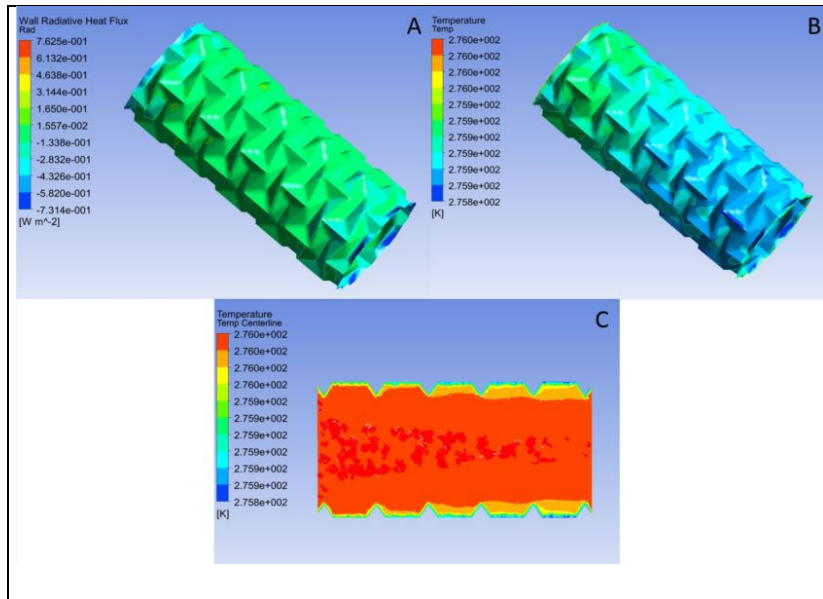
Figure 6.17 Thermal contour plots for Huffman Stars-Triangles
pattern at 63 % fold at 173 K. A is the radiation flux through the
fluid wall, B is the temperature on the fluid wall, and C is the
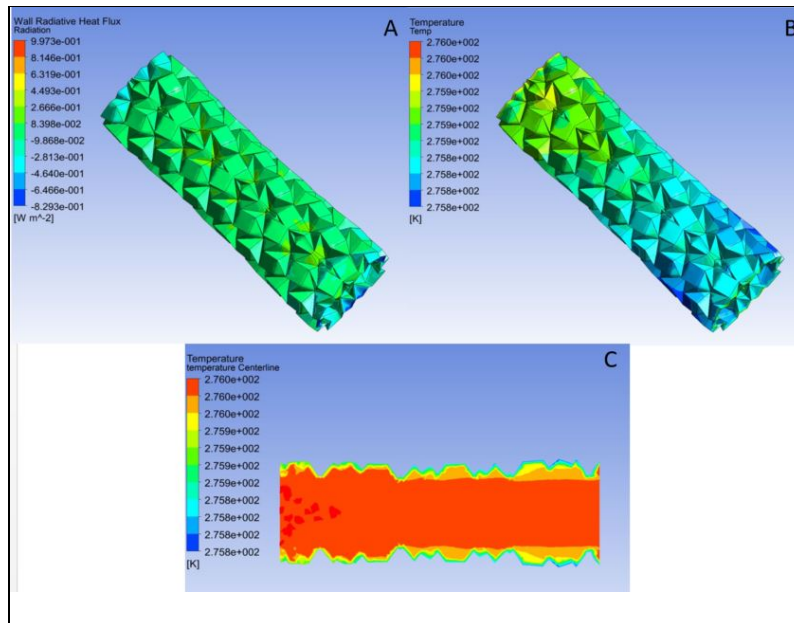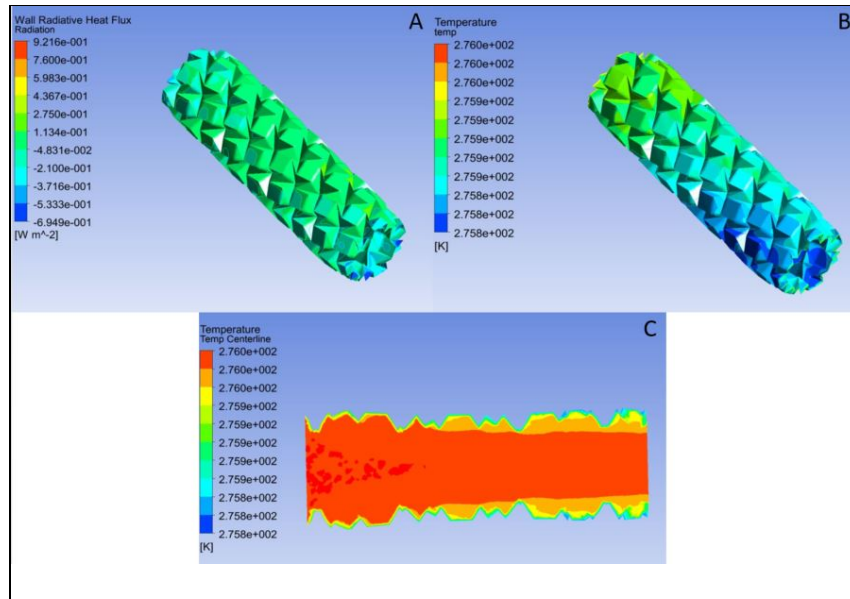centerline temperature.

The plot of the centerline temperature for all thee plots shows the formation of the

boundary layer similar to the Waterbomb and Huffman Waterbomb patterns. However, it was

much easier to define the locations. At 48 percent fold, the boundary layer formed after one fin.

At 54 percent fold and 63 percent fold, the boundary layer formed after two fins. The boundary

layer was also much thicker at 63 percent. The temperature plots of the fluid walls followed the

trend of the centerline. Areas with small boundary conditions were hotter than areas with large

boundary conditions. Like the Huffman Waterbomb pattern, the radiation flux from the surface

body was more unifrom than the temperature profile shown in the plot.

The velocity, temperature, and radiation plots are useful for understanding the physics of

the problem, as well as for validating the computational solution. Ultimately, what was of intrest

was the radiation output per unit of surface area (the surface being the fluid wall). I ran

simulations on all three patterns, varying the fold angle as described in Table 3.1. Each model

36

was simulated at a range of ambitent temperatures starting at 173 K and ending at 394 K.

Appendix D contains the results: the surface area of each model, the total radiation flux, and the

radiation flux per unit area.

CHAPTER 7: CONCLUSIONS AND FUTURE WORK

Chapter 6 and Appendix C present the graphic and numerical results of the simulations.
This chapter presents the analysis of that data, a conclusion about which pattern of the three
tested was best, and proposed future work to further probe the problem.

7.1 Radiation Flux Plots

I created plots of the radiation flux per unit area versus ambient temperature, as well as
radiation flux unit area versus fold percent for each of the patterns. Figure 7.1 to Figure 7.6
display the results for each pattern.
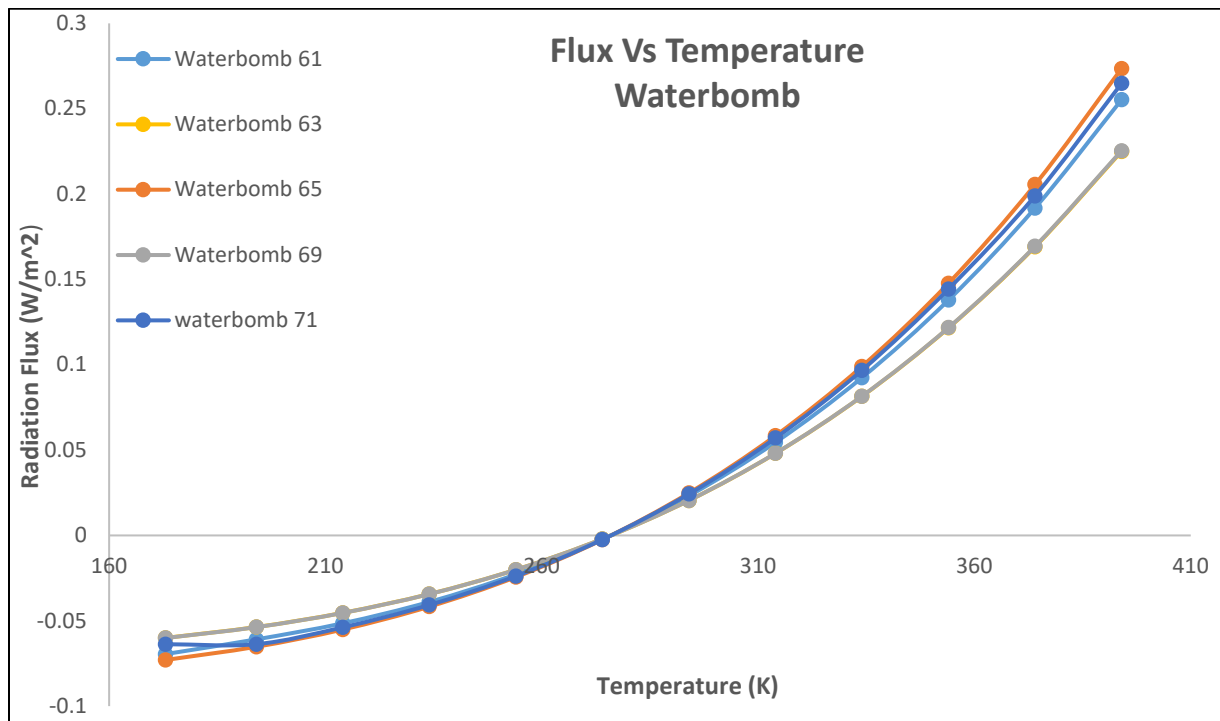
Figure 7.1 Plot of flux vs temperature for the Waterbomb pattern.

Figure 7.2 Plot of flux vs temperature for the Huffman Waterbomb pattern.
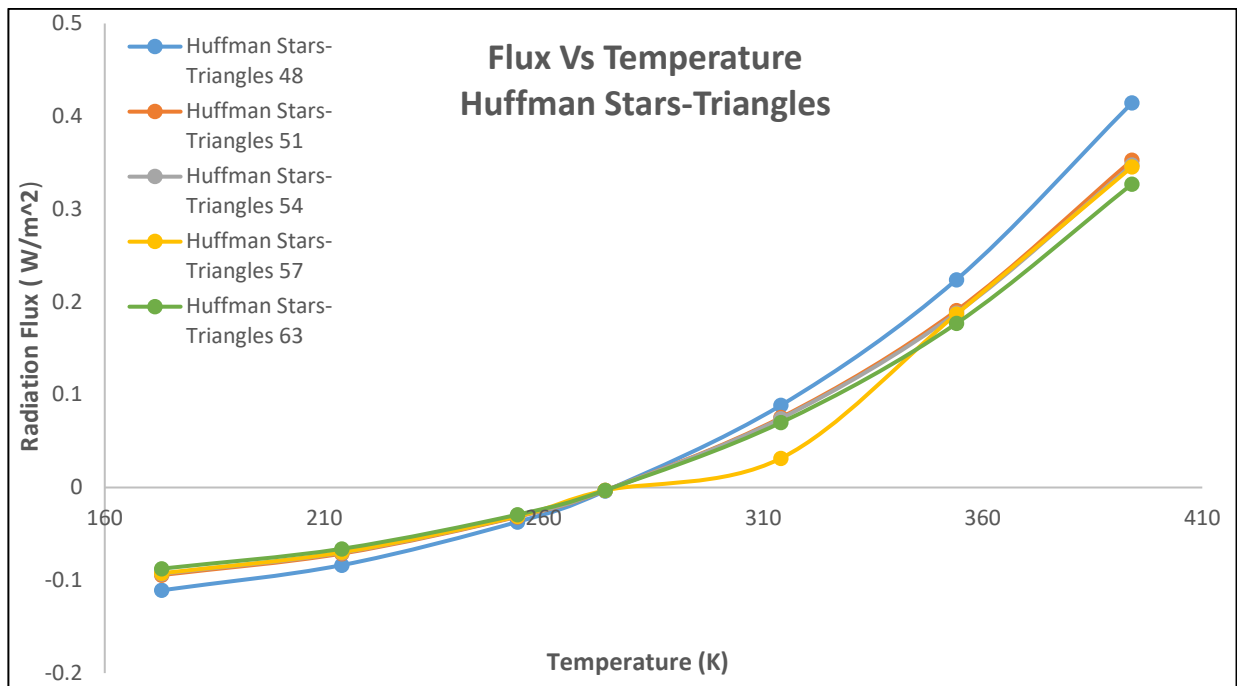
Figure 7.3 Plot of flux vs temperature for the Huffman Stars-Triangles pattern.

The three figures show that each configuration of the three patterns follows the same profile. The small deviations, such as for the data point at 314 K for the Huffman Stars-Triangles pattern at 57 percent fold, were caused by deviations in the geometries discussed in Chapter 3. The three models also show a common feature at the 274 K data point. Here, the radiation flux was essentially zero because the temperature of the working fluid was close to ambient (276 K). Thus, since the thermal gradient was small, there was little heat transfer.
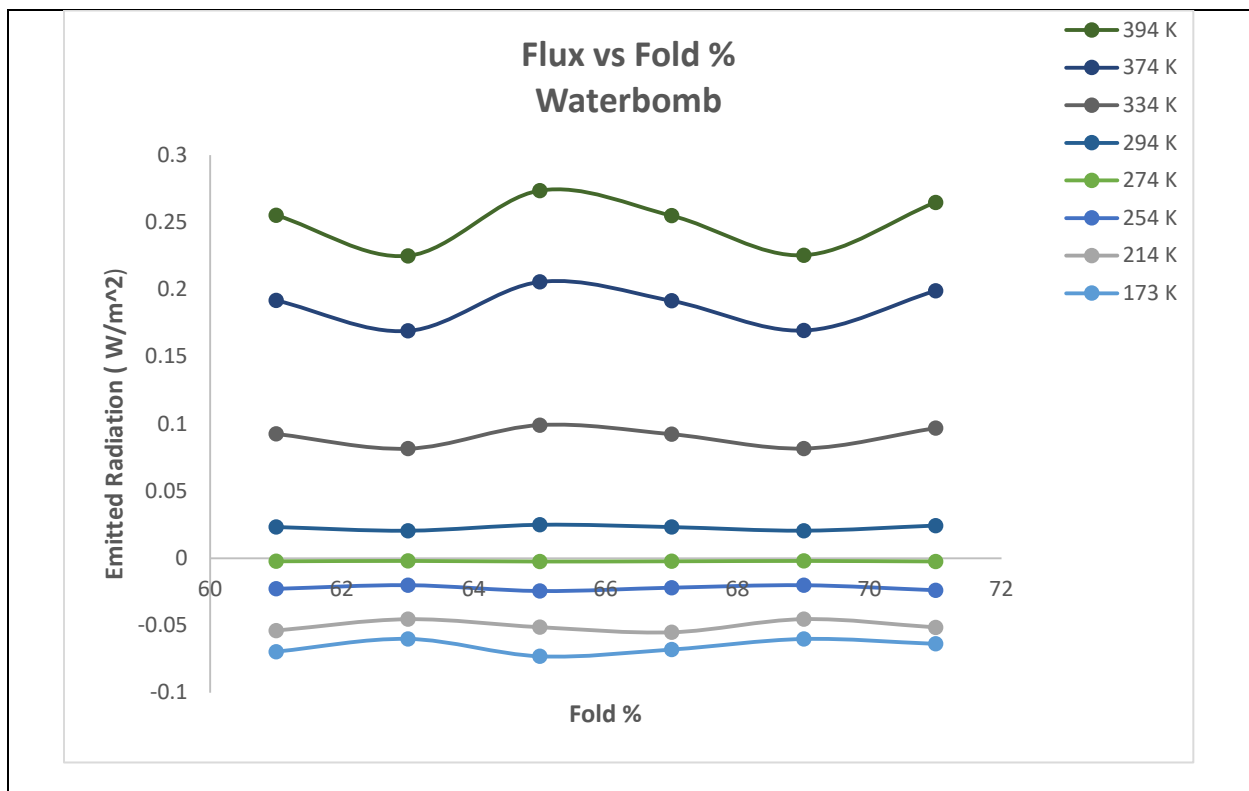
Figure 7.4 Plot of flux vs fold % for the Waterbomb pattern.

Figure 7.4, Figure 7.5, and Figure 7.6 are the most important plots. They show the radiation flux through the Fluid Wall as a function of fold percentage. Each of these plots shows that at a fixed temperature, as the fold percent was varied, the radiation flux changed. This is exactly the effect I hypothesized.
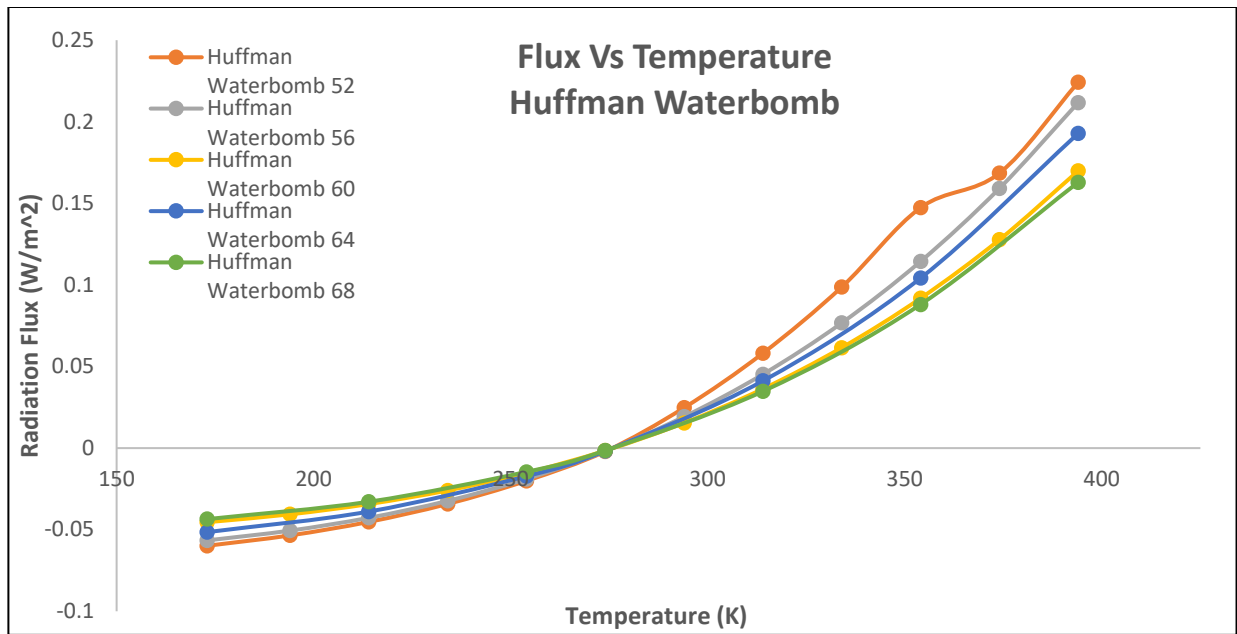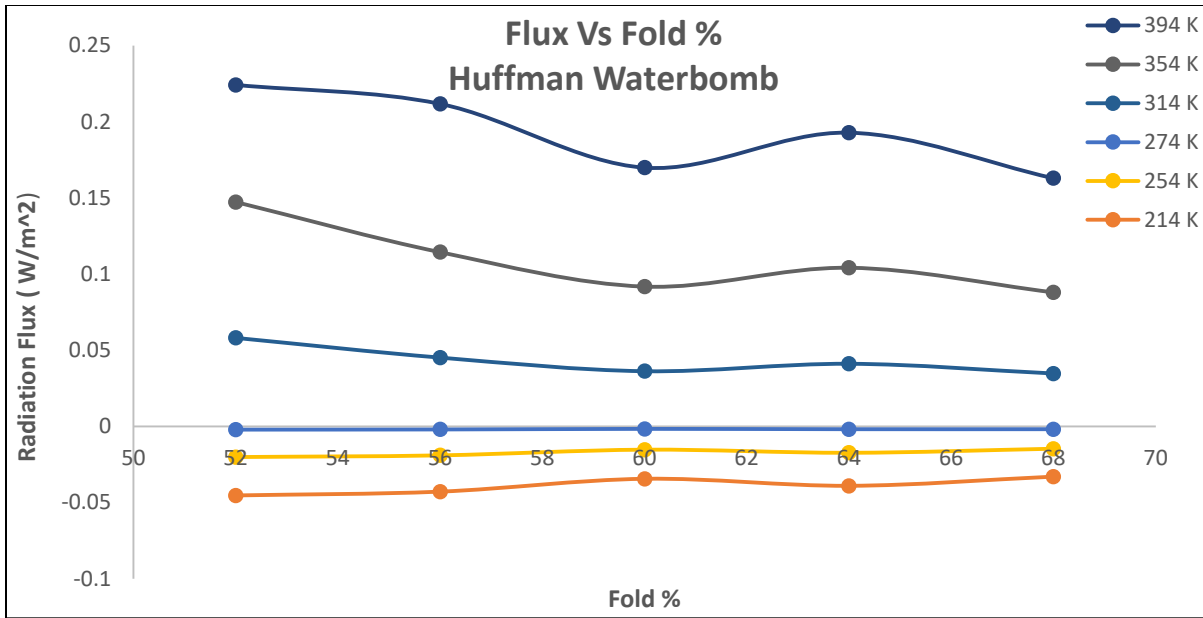
Figure 7.5 Plot of flux vs fold % for the Huffman Waterbomb pattern.
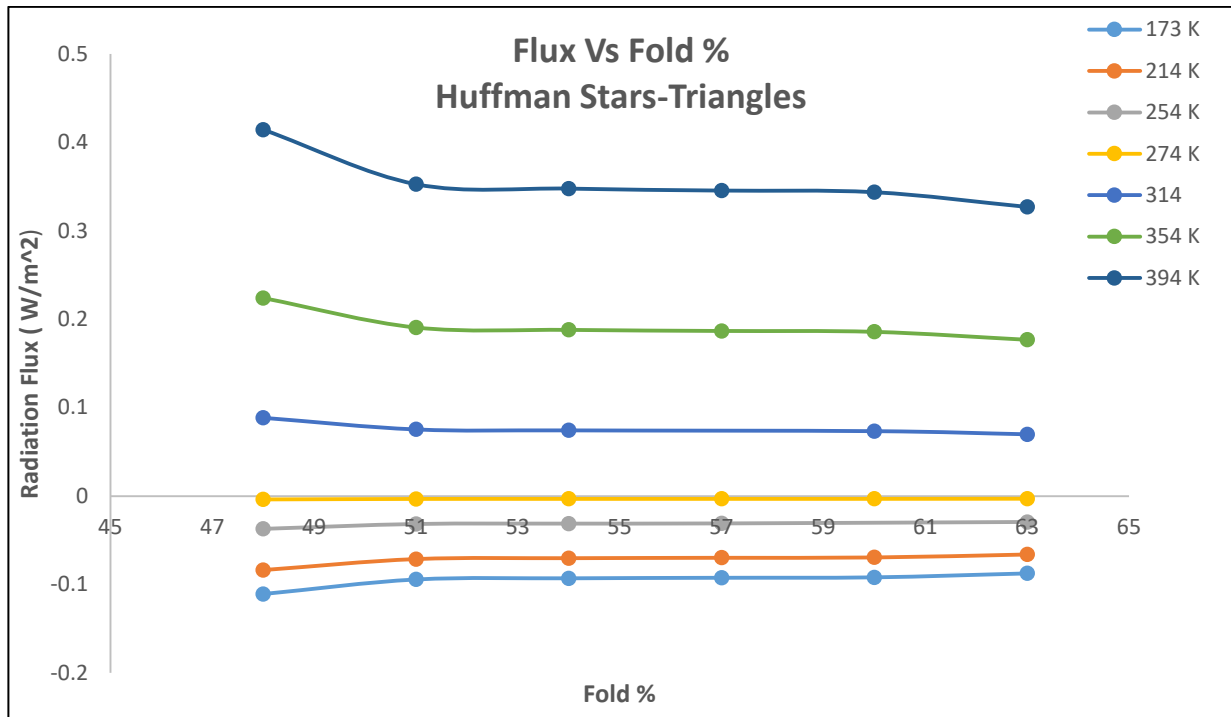
Figure 7.6 Plot of flux vs fold % for the Huffman Stars-Triangles pattern.

The change became small as the ambient temperature approched the temperature of the working fluid; the trend lines become flat here. This was again because the small thermal gradiant was independent of fold percent. In contrast, as the temperature difference became large, the fold percent had an impact on the radiation flux. This effect was not reflected across the temperature of the working fluid. At temperatures higher than that of the working fluid, the effect of fold percent contributed much more than at temperatures lower than that of the working fluid. The trend lines were also not monotomic. They showed valleys and peaks. These turning points correspond to the bodies reaching their maximum amount of foldedness. The Waterbomb pattern displayed the most sensitivity to fold percent (the curves reached the turning points in the smallest amounts of change of fold), followed by the Huffman Waterbomb. The Huffman Stars-Triangles pattern showed little sensitivty to fold percent; the trend lines were flat. This is because the cavities on the surface were too small to cause an appreciable cavity effect. It was still unclear whether the cavity effect or conduction in the shell along with conduction in the fluid were the dominating factors in the Waterbomb and Huffman Waterbomb patterns.

Examining the range of flux vs fold percent for the Huffman Waterbomb and Waterbomb pattens showed that Huffman Waterbomb had the greatest difference of radiation flux. At 394 K, the maximum radiation flux was 0.284 W/m^2 and the minimum was 0.162 W/m^2. This represented a difference of 42.7 %. This variation was over 20 percent of fold – the entire tested range. At 394 K, the Waterbomb pattern maximum radiation flux was 0.273 W/m^2 and the minimum was 0.225 W/m^2. This represented a difference of 17.6 percent. While the difference in flux was much less than that for the Huffman Waterbomb, the fold range was only two percent. Either of these two patterns is a suitable choice for a space based defromable radiator. Since they have different desierable properties, a wide range of radiation flux for the Huffman Waterbomb

42

and a sensitive fold dependence for the Waterbomb pattern, the choice of design would depend on other parameters, such as the orbit of the bodies, the duration needed for the radiator to reach equilibrium, ect.

7.2 Future Work

Future work should focus on the Waterbomb and Huffman Waterbomb patterns. First, the same type of simulations should be conducted with solid models that accounts for the overlap in the surface bodies, uses a finer mesh especially close to the Fluid Walls, and tightens convergence criteria. These should be analyzed for solid bodies with a smaller fold percentage sampling rate to better define the radiation flux versus the fold percentage curve.

ANSYS FLUENT has a built-in solar load model. On future simulations, this model should be used to simulate the incoming energy delivered by the sun as well as the Earth. Further simulations should also explore the effects of different working fluids, wall thickness, and wall materials.

The solid geometries that I used in my simulations were about 178.4 mm long. This dimension represented a small section of the radiator. A simulation of the flow through longer tubes should be done to study the effects of drag and turbulence on the flow far from the opening. Finally, working models of the design should be constructed to test the validity of the simulations and further refine them as needed.

CHAPTER 8: THESIS CONTRIBUTIONS

This thesis offers a controlable alternative to the static radiators curently being employed in large spacecraft by employing origami construction. I conducted and generated simulations for the fluid flows, temperature distrubitions, and radiation flux. I analyzed the radiation flux as a function of the fold percent of the bodies. I found the Waterbomb and the Huffman Waterbomb were the best candidates for an origami tube radiator, exhibiting as much as a 42.7 percent difference in expelled radiaton over the various configureations. Ultimately, this thesis has demonstrated that an origami radiatior has the ability to control the amount of energy radiation by deforming the topology of the body.

44

WORKS CITED

[1] R. B. Mulford and M. R. Jones, "Iverson B.D. Dynamic Control of Radiative Surface Properties With Origami-Inspired Design," ASME. *J Heat Transfer*, vol. 138, no. 3, March 2016. [Online]. Available: http://heattransfer.asmedigitalcollection.asme.org/. [January 24, 2018].

[2] M. M. Finckeno, and K. K. deGroh, *The International Space Station (ISS) Researcher's Guide Space Environmental Effects,* NASA ISS Program Science Office, 2015. [E-book] Available: https://www.nasa.gov/sites/default/files/files/NP-2015-03-015-JSC_Space_Environment-ISS-Mini-Book-2015-508.pdf

[3] A. Shternfeld, "*On Board an Artificial Satellite,*" in *Soviet Space Science*, 2nd edition. New York: Basic Books, Inc., 1959, pp. 210-211.

[4] Boeing, "Active Thermal Control Systems (ATCS) Overview," IDS Business Support, Communications and Community Affairs St. Louis, MO. [Online]. Available: https://www.nasa.gov/pdf/473486main_iss_atcs_overview.pdf. [Accessed June 1, 2018].

[5] R. Lang. "*Introduction,*" in *Origami Design Secrets*. 2nd edition. Boca Raton: CRC Press, 2011, pp. 3-6.

[6] N. Turner, B. Goodwine, M. Sen. "A review of origami application sin mechanical engineering," Journal of Mechanical Engineering Science. 230(14), 2345-2362, 2016.

[7] L. Keesey, "NASA's New Shape-Shifting Radiator Inspired by Origami," NASA's Goddard Space Flight Center Technology News. August 6, 2017. [Online]. Available: https://www.nasa.gov/feature/goddard/2017/nasa-s-new-shape-shifting-radiator-inspired-by-origami. [Accessed June 1, 2018].

[8] E. Davis, E. D. Demaine, M. L. Demaine, J. Ramseyer, (2018, October). "Reconstructing David Huffman's Origami Tessellations 1." *MIT Open Access Articles* [Online}. vol. 135, issue 11, Available: http://hdl.handel.net/1721.1/86200.

[9] H. T. Nguyen, P. T. Thai, B. Yu, I. Hagiwara, (2016, March). "Development of a Manufacturing Method for Truss Core Panels Based on Origami-Forming," *Journal of Mechanisms Robotics.* [Online]. vol 8, issue 3. Available: mechanismsrobotics.asmedigitalcollection.asme.org/article.aspx?articleid=2475685.

[10] G. S. Aglietti, M. Bandecchi, F. Chatel, et al., "Thermal Control of Spacecraft," in Spacecraft Systems Engineering, P. Fortescue, G. Swinerd, J. Stark, Eds. United Kingdom: John Wiley & Sons Ltd., 2011.

[11] ANSYS, Inc. ANSYS FLUENT User's Guide. (2013). [Online]. Canonsburg, PA: ANSYS, Inc. Available http://www.pmt.usp.br/ACADEMIC/martoran/NotasModelosGrad/ANSYS%20Fluent%20 Users%Guide.pdf, [Accessed June 1, 2018].

[12] S. Post, Applied and Computational Fluid Mechanics. Sudbury: Jones and Bartlett Publishers, 2011, pp. 164, 227.

[13] Wolfram|Alpha (2018). retrieved June 20, 2018, from http://www.wolframalpha.com/ with query "material properties."

[14] A. Ghassaei, "real-time origami simulation with VR Interface." Origami Simulation. [Online]. Available: http://www.amandaghassaei.com/projects/origami_simulator/, Accessed on: May 15, 2018.

[15] H. Lee, "Chatper 9 Meshing," in Finite Element Simulations with ANSYS Workbench 15 Theory, Applications, Case Studies", Mission, KS, USA: SDC Publications, 2014, ch 9 Meshing, sec. 9.1 Pneumatic Fingers, pp 327

APPENDIX A: SOLID MODEL DIMENSIONS

This Appendix contains all relevent dimentions for each solid model used.

Table A.1 Dimensions for each solid body.

Pattern	Fold %	Length, L (mm)	Outer Most Diameter, D (mm)	Fluid Wall Area, A (m²)
Waterbomb	61	178.2833	115.97273	0.125945
Waterbomb	63	178.416	109.42	0.129207
Waterbomb	65	178.48906	142.7859	0.17286
Waterbomb	67	178.36907	133.70439	0.177919
Waterbomb	69	178.38513	131.91988	0.1925
Waterbomb	71	178.4306	125.0676	0.223159
Huffman Waterbomb	48	178.62603	51.76799	0.352194
Huffman Waterbomb	52	178.412	50.574	0.0342905
Huffman Waterbomb	56	169.02	54.32634	0.035026
Huffman Waterbomb	60	178.02	54.04723	0.039515
Huffman Waterbomb	64	178.02	61.81313	0.047163
Huffman Waterbomb	68	178.42896	62.28951	0.052165
Huffman Stars-Triangles	48	178.43	85.7551	0.0508117
Huffman Stars-Triangles	51	178.4288	83.26753	0.049714
Huffman Stars-Triangles	54	178.4288	80.29634	0.0486459
Huffman Stars-Triangles	57	178.4172	83.0405	0.05078
Huffman Stars-Triangles	60	178.42976	85.67508	0.053175
Huffman Stars-Triangles	63	178.4288	88.12981	0.055752

APPENDIX B: MESH STATISTICS

This Appendix contains mesh information for each of the solid bodies. Listed in the number of elements, number of nodes and max skewness.

Table B.1 Mesh statistics for each solid body.

Pattern	Fold %	Number of Elements	Number of Nodes	Max Skewness
Waterbomb	61	135767	30199	0.97369
Waterbomb	63	120218	26462	0.92041
Waterbomb	65	160109	34089	0.85328
Waterbomb	67	142657	30842	0.88331
Waterbomb	69	156711	34332	0.94529
Waterbomb	71	263158	55539	0.93881
Huffman Waterbomb	48	174453	33293	0.93167
Huffman Waterbomb	52	218350	42237	0.94766
Huffman Waterbomb	56	124318	25230	0.94567
Huffman Waterbomb	60	252848	49406	0.89935
Huffman Waterbomb	64	144627	29669	0.8757
Huffman Waterbomb	68	399527	78185	0.93042
Huffman Stars-Triangles	48	212622	40991	0.93642
Huffman Stars-Triangles	51	200312	39104	0.85908
Huffman Stars-Triangles	54	114828	22870	0.92089
Huffman Stars-Triangles	57	111158	22126	0.89636
Huffman Stars-Triangles	60	114993	22937	0.89348
Huffman Stars-Triangles	63	291178	55840	0.94778

APPENDIX C: DYNAMIC FLOW PROPERTIES

This Appendix contains the dynamic flow properties descibred in the Chapter 2, the

Reynolds number and the entrance length.

Table C.1 Dynamic flow properties for each solid body

Pattern	Fold %	Length, L (mm)	Outer Most Diameter, D (mm)	Reynolds Number, Re	Entrance Length L_e (mm)
Waterbomb	61	178.2833	115.97273	6.12E+04	3202.970538
Waterbomb	63	178.416	109.42	5.77E+04	2992.842842
Waterbomb	65	178.48906	142.7859	7.53E+04	4082.604348
Waterbomb	67	178.36907	133.70439	7.05E+04	3781.299071
Waterbomb	69	178.38513	131.91988	6.96E+04	3722.485706
Waterbomb	71	178.4306	125.0676	6.60E+04	3497.894462
Huffman Waterbomb	48	178.62603	51.76799	2.73E+04	1249.901924
Huffman Waterbomb	52	178.412	50.574	2.67E+04	1216.334256
Huffman Waterbomb	56	169.02	54.32634	2.86E+04	1322.259223
Huffman Waterbomb	60	178.02	54.04723	2.85E+04	1314.337091
Huffman Waterbomb	64	178.02	61.81313	3.26E+04	1537.20554
Huffman Waterbomb	68	178.42896	62.28951	3.28E+04	1551.035781
Huffman Stars-Triangles	48	178.43	85.7551	4.52E+04	2252.203871
Huffman Stars-Triangles	51	178.4288	83.26753	4.39E+04	2176.169466
Huffman Stars-Triangles	54	178.4288	80.29634	4.23E+04	2085.848645
Huffman Stars-Triangles	57	178.4172	83.0405	4.38E+04	2169.248794
Huffman Stars-Triangles	60	178.42976	85.67508	4.52E+04	2249.752216
Huffman Stars-Triangles	63	178.4288	88.12981	4.65E+04	2325.132586

APPENDIX D: FLUX RESULTS

This Appendix contains the the amount of emitted radiation, and emitted radiation per unit area for each of the simulations run.

Table D.1 Flux data for each simulation.

Shape	Fold %	Surface Area (m^2)	Ambient Temperature (K)	Radiation Power (W)	Radiation Flux (W/m^2)
Waterbomb	61	0.125945	173	-0.008755015	-0.06951459
Waterbomb	61	0.125945	194	-0.007671097	-0.060908309
Waterbomb	61	0.125945	214	-0.006481363	-0.051461852
Waterbomb	61	0.125945	234	-0.004906412	-0.038956783
Waterbomb	61	0.125945	254	-0.002870584	-0.022792362
Waterbomb	61	0.125945	274	-0.000291224	-0.002312314
Waterbomb	61	0.125945	294	0.002921443	0.023196181
Waterbomb	61	0.125945	314	0.00686445	0.054503553
Waterbomb	61	0.125945	334	0.01164226	0.092439239
Waterbomb	61	0.125945	354	0.017367	0.137893525
Waterbomb	61	0.125945	374	0.02415871	0.191819524
Waterbomb	61	0.125945	394	0.03214571	0.255236095
Waterbomb	63	0.129207	173	-0.007758914	-0.06005026
Waterbomb	63	0.129207	194	-0.006936315	-0.05368374
Waterbomb	63	0.129207	214	-0.005860547	-0.045357813
Waterbomb	63	0.129207	234	-0.004436472	-0.034336158
Waterbomb	63	0.129207	254	-0.002595653	-0.020089105
Waterbomb	63	0.129207	274	-0.000263334	-0.002038082
Waterbomb	63	0.129207	294	0.00264168	0.020445332
Waterbomb	63	0.129207	314	0.006207164	0.048040462
Waterbomb	63	0.129207	334	0.01052761	0.081478635
Waterbomb	63	0.129207	354	0.01570451	0.12154535
Waterbomb	63	0.129207	374	0.02184645	0.16908101
Waterbomb	63	0.129207	394	0.02906963	0.224984947
Waterbomb	65	0.17286	173	-0.01261529	-0.07297981
Waterbomb	65	0.17286	194	-0.01127788	-0.065242855
Waterbomb	65	0.17286	214	-0.009528868	-0.055124771

Table D.1 (Continued)

Shape	Fold %	Surface Area (m^2)	Ambient Temperature (K)	Radiation Power (W)	Radiation Flux (W/m^2)
Waterbomb	65	0.17286	234	-0.007213472	-0.04173014
Waterbomb	65	0.17286	254	-0.004220447	-0.024415406
Waterbomb	65	0.17286	274	-0.000428179	-0.002477026
Waterbomb	65	0.17286	294	0.004295427	0.024849167
Waterbomb	65	0.17286	314	0.0100932	0.058389448
Waterbomb	65	0.17286	334	0.01711898	0.099033785
Waterbomb	65	0.17286	354	0.02553795	0.147737765
Waterbomb	65	0.17286	374	0.03552709	0.205525223
Waterbomb	65	0.17286	394	0.04727566	0.273491033
Waterbomb	67	0.177919	173	-0.01209106	-0.067958228
Waterbomb	67	0.177919	194	-0.01080953	-0.060755344
Waterbomb	67	0.177919	214	-0.009133223	-0.051333601
Waterbomb	67	0.177919	234	-0.006671853	-0.037499385
Waterbomb	67	0.177919	254	-0.003903616	-0.021940411
Waterbomb	67	0.177919	274	-0.000410431	-0.002306844
Waterbomb	67	0.177919	294	0.004117442	0.023142228
Waterbomb	67	0.177919	314	0.009675651	0.054382337
Waterbomb	67	0.177919	334	0.01641145	0.092241132
Waterbomb	67	0.177919	354	0.02448457	0.137616387
Waterbomb	67	0.177919	374	0.0340641	0.191458473
Waterbomb	67	0.177919	394	0.04533311	0.25479634
Waterbomb	69	0.1925	173	-0.0115719	-0.060113766
Waterbomb	69	0.1925	194	-0.01034521	-0.053741351
Waterbomb	69	0.1925	214	-0.008740961	-0.04540759
Waterbomb	69	0.1925	234	-0.006617158	-0.034374847
Waterbomb	69	0.1925	254	-0.003871655	-0.020112494
Waterbomb	69	0.1925	274	-0.000392806	-0.002040548
Waterbomb	69	0.1925	294	0.003940729	0.020471319
Waterbomb	69	0.1925	314	0.009260209	0.048104982
Waterbomb	69	0.1925	334	0.01570709	0.081595273
Waterbomb	69	0.1925	354	0.0234334	0.121731948
Waterbomb	69	0.1925	374	0.03260217	0.169361922
Waterbomb	69	0.1925	394	0.04338783	0.225391325
Waterbomb	71	0.223159	173	-0.01422101	-0.063725908
Waterbomb	71	0.223159	194	-0.01422101	-0.063725908
Waterbomb	71	0.223159	214	-0.01201577	-0.053843986
Waterbomb	71	0.223159	234	-0.009096423	-0.040762071
Waterbomb	71	0.223159	254	-0.005322384	-0.023850188

Table D.1 (Continued)

Shape	Fold %	Surface Area (m^2)	Ambient Temperature (K)	Radiation Power (W)	Radiation Flux (W/m^2)
Waterbomb	71	0.223159	274	-0.000539993	-0.002419768
Waterbomb	71	0.223159	294	0.005417628	0.024276986
Waterbomb	71	0.223159	314	0.0127312	0.057049906
Waterbomb	71	0.223159	234	-0.009096423	-0.040762071
Waterbomb	71	0.223159	254	-0.005322384	-0.023850188
Waterbomb	71	0.223159	274	-0.000539993	-0.002419768
Waterbomb	71	0.223159	294	0.005417628	0.024276986
Waterbomb	71	0.223159	314	0.0127312	0.057049906
Waterbomb	71	0.223159	334	0.02159539	0.096771316
Waterbomb	71	0.223159	354	0.03221942	0.144378761
Waterbomb	71	0.223159	374	0.04439578	0.198942368
Waterbomb	71	0.223159	394	0.05908618	0.264771665
Huffman Waterbomb	48	0.0352194	173	-0.00267197	-0.075866426
Huffman Waterbomb	48	0.0352194	194	-0.005029441	-0.142803143
Huffman Waterbomb	48	0.0352194	214	-0.004249298	-0.120652197
Huffman Waterbomb	48	0.0352194	234	-0.003740959	-0.106218703
Huffman Waterbomb	48	0.0352194	254	-0.002189396	-0.062164489
Huffman Waterbomb	48	0.0352194	274	-0.000222206	-0.006309188
Huffman Waterbomb	48	0.0352194	294	0.002230176	0.063322373
Huffman Waterbomb	48	0.0352194	314	0.005243376	0.148877494
Huffman Waterbomb	48	0.0352194	334	0.00889943	0.252685452
Huffman Waterbomb	48	0.0352194	354	0.01328718	0.377268778
Huffman Waterbomb	48	0.0352194	374	0.01850226	0.525342851
Huffman Waterbomb	48	0.0352194	394	0.01000779	0.284155607
Huffman Waterbomb	52	0.0342905	173	-0.002052697	-0.059861973
Huffman Waterbomb	52	0.0342905	194	-0.001835056	-0.053514997

www.manaraa.com

Table D.1 (Continued)

Shape	Fold %	Surface Area (m^2)	Ambient Temperature (K)	Radiation Power (W)	Radiation Flux (W/m^2)
Huffman Waterbomb	52	0.0342905	214	-0.001550441	-0.045214885
Huffman Waterbomb	52	0.0342905	234	-0.001173676	-0.034227439
Huffman Waterbomb	52	0.0342905	254	-0.000686673	-0.020025156
Huffman Waterbomb	52	0.0342905	274	-6.97E-05	-0.002031545
Huffman Waterbomb	52	0.0342905	294	0.000848599	0.024747356
Huffman Waterbomb	52	0.0342905	314	0.001994806	0.058173722
Huffman Waterbomb	52	0.0342905	334	0.003385032	0.098716321
Huffman Waterbomb	52	0.0342905	354	0.005052754	0.147351424
Huffman Waterbomb	52	0.0342905	374	0.005778045	0.168502792
Huffman Waterbomb	52	0.0342905	394	0.00768792	0.224199705
Huffman Waterbomb	56	0.035026	173	-0.001981127	-0.056561611
Huffman Waterbomb	56	0.035026	194	-0.001771062	-0.050564209
Huffman Waterbomb	56	0.035026	214	-0.001496352	-0.042721179
Huffman Waterbomb	56	0.035026	234	-0.001132713	-0.032339205
Huffman Waterbomb	56	0.035026	254	-0.000662694	-0.018920059
Huffman Waterbomb	56	0.035026	274	-6.72E-05	-0.001919375
Huffman Waterbomb	56	0.035026	294	0.000674366	0.019253283
Huffman Waterbomb	56	0.035026	314	0.001584435	0.045235968
Huffman Waterbomb	56	0.035026	334	0.002687021	0.07671504
Huffman Waterbomb	56	0.035026	354	0.004007899	0.114426398
Huffman Waterbomb	56	0.035026	374	0.005574648	0.159157426

Table D.1 (Continued)

Shape	Fold %	Surface Area (m^2)	Ambient Temperature (K)	Radiation Power (W)	Radiation Flux (W/m^2)
Huffman Waterbomb	56	0.035026	394	0.007416652	0.211747045
Huffman Waterbomb	60	0.039515	173	-0.001794235	-0.045406428
Huffman Waterbomb	60	0.039515	194	-0.001603963	-0.040591244
Huffman Waterbomb	60	0.039515	214	-0.001355147	-0.034294496
Huffman Waterbomb	60	0.039515	234	-0.0010258	-0.025959762
Huffman Waterbomb	60	0.039515	254	-0.000600126	-0.015187288
Huffman Waterbomb	60	0.039515	274	-6.09E-05	-0.001540645
Huffman Waterbomb	60	0.039515	294	0.000610648	0.015453577
Huffman Waterbomb	60	0.039515	314	0.001434648	0.036306415
Huffman Waterbomb	60	0.039515	334	0.002432835	0.061567379
Huffman Waterbomb	60	0.039515	354	0.003628469	0.091825104
Huffman Waterbomb	60	0.039515	374	0.005046386	0.127708111
Huffman Waterbomb	60	0.039515	394	0.00671309	0.169887131
Huffman Waterbomb	64	0.047163	173	-0.002428456	-0.051490702
Huffman Waterbomb	64	0.047163	214	-0.001834263	-0.038891992
Huffman Waterbomb	64	0.047163	254	-0.000812379	-0.017224911
Huffman Waterbomb	64	0.047163	274	-8.24E-05	-0.001747467
Huffman Waterbomb	64	0.047163	314	0.001942557	0.041188156
Huffman Waterbomb	64	0.047163	354	0.004914406	0.104200454
Huffman Waterbomb	64	0.047163	394	0.009095763	0.192858024
Huffman Waterbomb	68	0.052165	173	-0.002270426	-0.043523934

54

Table D.1 (Continued)

Shape	Fold %	Surface Area (m^2)	Ambient Temperature (K)	Radiation Power (W)	Radiation Flux (W/m^2)
Huffman Waterbomb	68	0.052165	214	-0.001714854	-0.032873651
Huffman Waterbomb	68	0.052165	254	-0.000759459	-0.014558783
Huffman Waterbomb	68	0.052165	274	-7.70E-05	-0.001476941
Huffman Waterbomb	68	0.052165	314	0.001815794	0.034808665
Huffman Waterbomb	68	0.052165	354	0.004593112	0.088049688
Huffman Waterbomb	68	0.052165	394	0.008499533	0.162935551
Huffman Stars-Triangles	48	0.0508117	173	-0.005626025	-0.110723022
Huffman Stars-Triangles	48	0.0508117	214	-0.004249298	-0.083628338
Huffman Stars-Triangles	48	0.0508117	254	-0.001881857	-0.037035899
Huffman Stars-Triangles	48	0.0508117	274	-0.000190906	-0.003757125
Huffman Stars-Triangles	48	0.0508117	314	0.004499132	0.088545197
Huffman Stars-Triangles	48	0.0508117	354	0.01138013	0.223966724
Huffman Stars-Triangles	48	0.0508117	394	0.0210574	0.414420301
Huffman Stars-Triangles	51	0.049714	173	-0.004687633	-0.09429201
Huffman Stars-Triangles	51	0.049714	214	-0.00354043	-0.071215955
Huffman Stars-Triangles	51	0.049714	254	-0.001567845	-0.031537293
Huffman Stars-Triangles	51	0.049714	274	-0.000159045	-0.003199201
Huffman Stars-Triangles	51	0.049714	314	0.003747882	0.075388864
Huffman Stars-Triangles	51	0.049714	354	0.009478525	0.190661081
Huffman Stars-Triangles	51	0.049714	394	0.0175351	0.352719556
Huffman Stars-Triangles	54	0.0486456	173	-0.004521991	-0.092957863

Table D.1 (Continued)
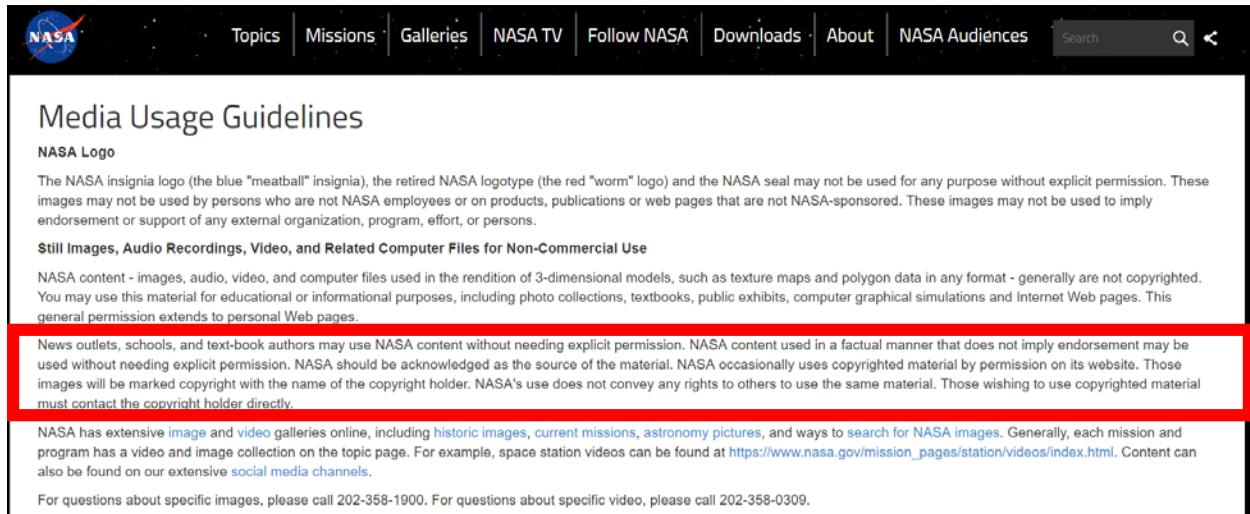
Shape	Fold %	Surface Area (m^2)	Ambient Temperature (K)	Radiation Power (W)	Radiation Flux (W/m^2)
Huffman Stars-Triangles	54	0.0486456	214	-0.003415349	-0.070208796
Huffman Stars-Triangles	54	0.0486456	254	-0.001512451	-0.031091219
Huffman Stars-Triangles	54	0.0486456	274	-0.000153426	-0.00315396
Huffman Stars-Triangles	54	0.0486456	314	0.003615504	0.074323351
Huffman Stars-Triangles	54	0.0486456	354	0.00914378	0.187967257
Huffman Stars-Triangles	54	0.0486456	394	0.01691603	0.347740186
Huffman Stars-Triangles	57	0.05078	173	-0.004690204	-0.092363214
Huffman Stars-Triangles	57	0.05078	214	-0.003542385	-0.069759453
Huffman Stars-Triangles	57	0.05078	254	-0.001568718	-0.030892438
Huffman Stars-Triangles	57	0.05078	274	-0.000159134	-0.003133797
Huffman Stars-Triangles	57	0.05078	314	0.001596189	0.031433419
Huffman Stars-Triangles	57	0.05078	354	0.009484027	0.186766975
Huffman Stars-Triangles	57	0.05078	394	0.01754561	0.345522056
Huffman Stars-Triangles	60	0.053175	173	-0.004884839	-0.091863451
Huffman Stars-Triangles	60	0.053175	214	-0.00368939	-0.06938204
Huffman Stars-Triangles	60	0.053175	254	0.009877764	0.185759549
Huffman Stars-Triangles	60	0.053175	274	-0.000165739	-0.003116856
Huffman Stars-Triangles	60	0.053175	314	0.00390567	0.073449365
Huffman Stars-Triangles	60	0.053175	354	0.009877764	0.185759549
Huffman Stars-Triangles	60	0.053175	374	0.01373748	0.258344711
Huffman Stars-Triangles	60	0.053175	394	0.0182742	0.343661495

56

Table D.1 (Continued)

Shape	Fold %	Surface Area (m^2)	Ambient Temperature (K)	Radiation Power (W)	Radiation Flux (W/m^2)
Huffman Stars-Triangles	63	0.055752	173	-0.004874438	-0.087430729
Huffman Stars-Triangles	63	0.055752	214	-0.003681512	-0.066033721
Huffman Stars-Triangles	63	0.055752	254	-0.001630317	-0.029242305
Huffman Stars-Triangles	63	0.055752	274	-0.000165382	-0.002966383
Huffman Stars-Triangles	63	0.055752	314	0.003897178	0.06990203
Huffman Stars-Triangles	63	0.055752	354	0.009855983	0.176782591
Huffman Stars-Triangles	63	0.055752	394	0.01823313	0.327039927

APPENDIX E: COPYRIGHT PERMISSIONS

E.1 Permission to Use Figure 2.1